INSTITUTE OF PHYSICS PUBLISHING REPORTS ON PROGRESS IN PHYSICS

Rep. Prog. Phys. **69** (2006) 181–232 doi:10.1088/0034-4885/69/1/R04

Fundamental physics of vacuum electron sources

Shigehiko Yamamoto

National Institute of Advanced Industrial Science and Technology (AIST), AIST Tsukuba Central 2, 1-1-1 Umezono, Tsukuba, Ibaraki 305-8568, Japan

Received 27 July 2005, in final form 19 October 2005
Published 21 November 2005
Online at stacks.iop.org/RoPP/69/181

Abstract

The history of electron emission is reviewed from a standpoint of the work function that determines the electron emission capability and of applications in the fields of scientific instruments and displays. For years, in thermionic emission, a great deal of effort has been devoted to the search for low work function materials with high melting temperature, while reduction of the local change in time of the work function rather than the work function itself has been the main issue of field emission investigations. High brightness and long life are the central targets of emission material investigations for scientific instrument applications, while high current density and low power consumption are the guiding principles for display applications.

In most of the present day industries, thermionic emission materials are exclusively used in such fields requiring high current and high reliability as cathode ray tubes, transmission and receiving tubes, x-ray sources and various electron beam machines. Field electron emission sources, however, since applied to high resolution electron microscopes in the 1970s have recently become dominant in research and development in the fields of scientific instruments as well as in the fields of various electron tubes and beam machines.

The main issue in this report is to analyse the work function on the atomic scale and thereby to understand the fundamental physics behind the work function, the change in time of the local work function leading to field emission current fluctuation and the relationship between microscopic (on atomic scale) and macroscopic work functions.

Our attempt is presented here, where the work function on the atomic scale is measured by utilizing a scanning tunnelling microscopy technique, and it is made clear how far the local work function extends its influence over neighbouring sites. As a result, a simple relationship is established between microscopic and macroscopic work functions.

Contents

	Page
1. Introduction	184
2. Electron emission and work function	184
2.1. Thermionic emission	184
2.2. Field emission	185
2.3. Field emission under extreme conditions	185
3. Work function	188
3.1. Work function—definition	188
3.2. Work function based on phenomenological relations	189
3.2.1. Work function of single elements	189
3.2.2. Work function of binary compounds AB	189
3.2.3. Work function change due to adsorption of atoms and molecules	191
3.2.4. Work function of surface monolayer cathode	193
3.3. Work function on the atomic scale	194
3.3.1. Work function on the atomic scale, definition	194
3.3.2. Work function measurements on the atomic scale	195
3.3.3. Relationship between macroscopic and microscopic work functions	195
3.4. Theoretical aspect of work function	198
3.4.1. Work function of single elements (theory)	198
3.4.2. Work function of binary compounds (theory)	199
3.4.3. Work function of a monolayer (theory)	200
4. Historical review of thermionic emission materials	201
4.1. Tungsten and thoriated tungsten cathodes	201
4.2. Lanthanum hexabaride (LaB_6) cathodes	201
4.3. Oxide cathodes	203
4.3.1. Oxide cathode structure	203
4.3.2. Work function of oxide cathodes	204
4.3.3. Electron conduction mechanism of oxide cathodes	206
4.3.4. High current density oxide cathode	207
4.4. High current density cathodes	207
4.4.1. L cathode and its derivatives	208
4.4.2. Impregnated cathodes and their derivatives	208
4.4.3. Scandate cathode	211
4.4.4. Theoretical aspects of cathode operation	213
5. Historical review of field emission materials	216
5.1. History of field emission materials	217
5.2. Field emission current fluctuation from metal field emitters	218
5.2.1. Flicker noise type current fluctuation	218
5.2.2. Theoretical aspect of flicker noise type current fluctuation	220
5.3. Field emission from carbon materials	223
5.3.1. Step and spike type current fluctuation	223

5.3.2. Mechanism of step and spike type current fluctuation 225
5.4. Reduction of current fluctuation by ensemble averaging 228
6. Summary 228
Acknowledgments 229
References 229

1. Introduction

In spite of its long history of over a century and although it has been utilized in a variety of fields, the details of electron emission, however, have not yet been disclosed beyond the old concepts. There are, however, many fields of nanotechnology in which the old concepts have now become meaningless. Since electron emission has rarely been discussed on an atomic scale, it is urgent and important for us to make clear the fundamental physics in electron emission by applying modern concepts as well as appropriate advanced scientific techniques. In this report, the author wishes to approach the core of electron emission, focusing both on thermionic and field electron emission, because only these two electron emission types have been widely used in vacuum electronics, excluding other electron emission types such as photoelectron emission, secondary electron emission and so on.

The relationship between electron emission and the work function that determines electron emission capabilities will briefly be described in section 2, while the details of the work function are discussed in section 3. The historical development of thermionic emission and field electron emission will be presented in sections 4 and 5, respectively. Section 6 is the summary.

2. Electron emission and work function

2.1. Thermionic emission

In thermionic emission, electrons in solids carrying enough energy to overcome the potential barrier, referred to as the work function, can escape into vacuum. Due to the wave nature of electrons, some electrons with enough energy to overcome the barrier, however, have a chance to return to the solid and do not contribute to electron emission.

The thermionic saturation emission current density from metals is derived by Richardson in 1912 [1] as

$$J_s = \frac{4\pi mek^2T^2}{h^3}\exp\left(-\frac{\phi}{kT}\right) = AT^2\exp\left(-\frac{\phi}{kT}\right), \tag{1}$$

where $A = 4\pi mek^2/h^3$ is the Richardson constant, T the temperature and ϕ the work function.

Until the birth of the oxide cathode, tungsten (W) had widely been utilized as a typical thermionic emission material. As is well known nowadays, the oxide cathode is superior to all other thermionic emissive materials in a number of aspects. In the early 1900s Wehnelt discovered by chance that certain alkali-earth oxide materials show an excellent thermionic electron emission capability [2]. The oxide material mainly composed of BaO has since been widely used for a century after its discovery. The oxide cathode is an n-type semiconductor with oxygen vacancies that are created by reducing BaO. The electron emission current density from an oxide cathode was first proposed by Wilson [3] and then was modified by Nottingham [4] as

$$J_s = n_D^{1/2}\frac{e\sqrt{2}(2\pi m)^{1/4}k^{5/4}}{h^{3/2}}T^{5/4}\exp\left(-\frac{\phi}{kT}\right), \tag{2}$$

where n_D is the donor concentration. The major difference from the Richardson equation is that the donor concentration n_D is included in the expression. Here, $\phi = \chi + (E_D/2)$, where χ is the electron affinity and E_D the energy of the donor level measured from the bottom of the conduction band.

2.2. Field emission

Field emission is the quantum mechanical tunnelling to vacuum of electrons in solids through the work function potential barrier. Tunnelling was discovered in the early 1920s and theoretically confirmed in the late 1920s. Field emission has been utilized for a high brightness electron source since the first instalment to electron microscopes in the 1970s. Today, field emission is reported to be observed from single atoms, carbon nano-tubes (CNTs) and even from superconductive materials.

The field emission current density is formulated by the following steps: (1) firstly, the electron flux in the solid moving towards vacuum (x-direction), referred to as the supply function, is computed based on statistical mechanics, (2) the probability is computed for the electrons hitting the potential barrier, the work function barrier, to get through by tunnelling and (3) by combining the above two, the field emission current density can be obtained as a function of the applied electric field F as

$$J_0 = \frac{e^2F^2}{8\pi\phi ht^2(y)} \exp\left[\frac{-4\sqrt{2m}\phi^{3/2}v(y)}{3e\hbar F}\right] = \frac{AF^2}{\phi}\exp\left(-\frac{B\phi^{3/2}}{F}\right), \tag{3}$$

where $A = e^2/8\pi ht^2(y)$ and $B = 4\sqrt{2m}v(y)/3e\hbar$ are slowly varying functions of $y = \sqrt{e^3F}/\phi$ [5]. This is the equation for the field emission current density originally derived by Fowler and Nordheim [6,7] and later modified by Murphy and Good [5].

The energy distribution of field emitted electrons is given as

$$J(\varepsilon) = \frac{J_0 f(\varepsilon)\exp(\varepsilon/d)}{d} = \frac{J_0\exp(\varepsilon/d)}{d[1+\exp(\varepsilon/pd))]}, \tag{4}$$

where $\varepsilon = E - E_F$, the energy with respect to the Fermi energy. In this expression the free electron model is assumed in the solid and hence the Fermi–Dirac distribution is adapted as follows:

$$f(\varepsilon) = \frac{1}{1+\exp(\varepsilon/pd)}, \tag{5}$$

where $p = kT/d$ and

$$\frac{1}{d} = \frac{2\sqrt{2m\phi}t(y)}{\hbar eF}. \tag{6}$$

The field emission current density J_0 in (3) is obtained by integrating (4) over all ε at 0 K.

2.3. Field emission under extreme conditions

The Fowler–Nordheim equation is based on the following approximations: (1) a one-dimensional model is assumed for the electron source, (2) the energy band structure in the solid is neglected, (3) tunnelling is restricted to the energy region very near the Fermi energy, (4) free electrons are assumed in the solid and (5) the WKB method is adapted in calculating the tunnelling probability.

The calculation based on three-dimensional source structures has revealed that there is not much difference in the results between one-dimensional and three-dimensional sources [8]. However, the source structure on an atomic scale becomes essential in such a case as CNTs.

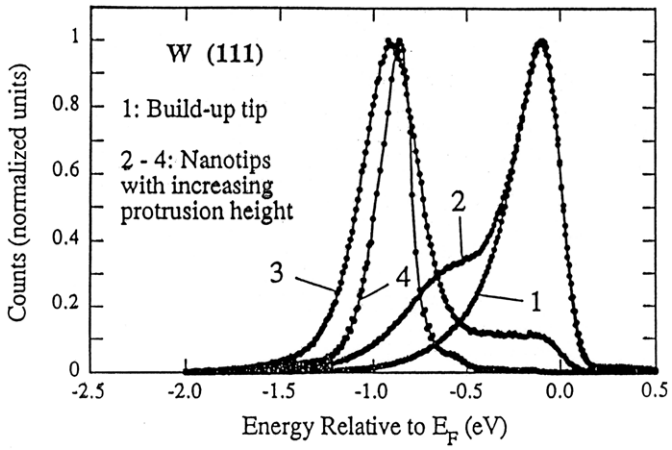

Figure 1. Energy distribution of field emitted electrons from a nano-tip on W(111) (after [11]).

Influence of energy band structures in the solid. Gadzuk computed the tunnelling probability in the case of d-band metals in which the Bloch wave approximation is more appropriate and found that the tunnelling probability is depressed by two to three orders of magnitude compared with the case of the s-band free electron approximation [9]. The energy distribution of field emitted electrons from a W(100) plane displays, in addition to the main peak near the Fermi level, an extra peak in a deep energy level [10]. Based on energy band calculations, the extra peak is attributed to the surface state originating from 5d-bands. In recent years, multiple peaks in the energy distribution have been revealed in the field emission from a single-atom tip [11] as well as from multi-walled CNTs (MWCNTs) [12].

Figure 1 shows the energy distribution of field emitted electrons from a W(111) plane. By building a single atom tip on top of the surface by the 'field surface melting' technique, the second peak appears in a deep level in the distribution spectrum in addition to the peak near the Fermi level [11]. The second peak moves into deeper levels as the electric field on the tip surface increases. Binh *et al* propose that the second peak is attributed to the resonance tunnelling through a localized band introduced by the single atom on the W(111) surface.

Resonance tunnelling has long been discussed in a framework of expanding the Fowler–Nordheim equation. Assuming a pseudo-energy level created by an atom that is located at Δ below the Fermi energy and has the Lorentian distribution with Γ of the full width at the half maximum (FWHM), Gadzuk [13] gave a simple straightforward expression for the energy distribution of field emitted electrons as

$$J^*(\varepsilon) = J(\varepsilon)\left[1 + \frac{T_r^2}{(\varepsilon-\Delta)^2+\Gamma^2} + \frac{2(\varepsilon-\Delta)T_r}{(\varepsilon-\Delta)^2+\Gamma^2}\right]. \tag{7}$$

Here T_r is the ratio of the tunnelling probability between the cases with an atom and without it. The first term on the right of the equation is due to direct tunnelling, the second term is due to resonance tunnelling and the third term represents the interference between direct and resonance tunnelling, respectively.

The energy distribution of field emitted electrons from a MWCNT also shows an extra peak, which moves with the electric field. The mobile peak is explained to be attributed to the resonance tunnelling through the localized energy level originating from the atom in the outermost wall of the MWCNT, while the immobile peak near the Fermi level is from the top of the valence band of inner walls of the MWCNT [12].

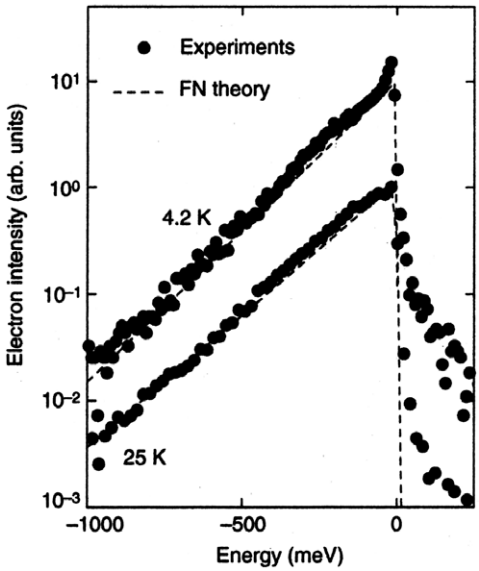

Figure 2. Energy distribution of field emitted electrons from Nb both above and below the critical temperature ($T_C = 9.2$ K) (after [15]).

Many body effect in solid. Analysis of field emission from superconductors was initiated by Gadzuk [14], who predicted that an extremely sharp peak on the order of 3 meV in the FWHM should appear near the Fermi energy. The sharp peak, however, had not been discovered from the time of his prediction until Oshima's group reported a small sharp peak superposed on the Fowler–Nordheim energy spectrum as shown in figure 2 [15]. By utilizing a high resolution electron energy analyser operable under an extremely high vacuum condition, they measured the energy distribution of field emitted electrons from a Nb superconductor operating at 4.2 K. The peak width measured, however, was 20 meV in the FWHM, far broader than Gadzuk's prediction. They explain that this may be due to the deterioration of the analyser's resolution during the experiment. They also add that the reason for failures to observe a sharp peak in the past may be the interruption of the electron emission from a superconductor due to adsorbed gas atoms on the superconducting surface.

Recent theories on field emission. Watanabe's group is developing a new theory of field emission based on first principles [16]. As a first step, by adapting a semi-infinite jellium as a field emission material, they have calculated self-consistently the change in the electron density distribution and the potential barrier created by the electron charge density. As for the tunnelling probability they have applied the recursion transfer matrix method developed by Hirose and Tsukada [17] and obtained the electron emission current density, which well reproduces the Fowler–Nordheim equation under relatively low field strength but deviates from it under strong electric field. According to this theory the tunnelling barrier height decreases with the electric field strength until reaching effectively no barrier height at $F = 10\,\mathrm{V\,nm^{-1}}$. The field emission current saturation under high field strength is, therefore, a result of the reduction in the tunnelling barrier height rather than the space charge effect as has been believed for a long time.

By extending the theory to include surface atomic structures, they have reported electron emission from a graphite ribbon with either zigzag or armchair structures [18]. The importance

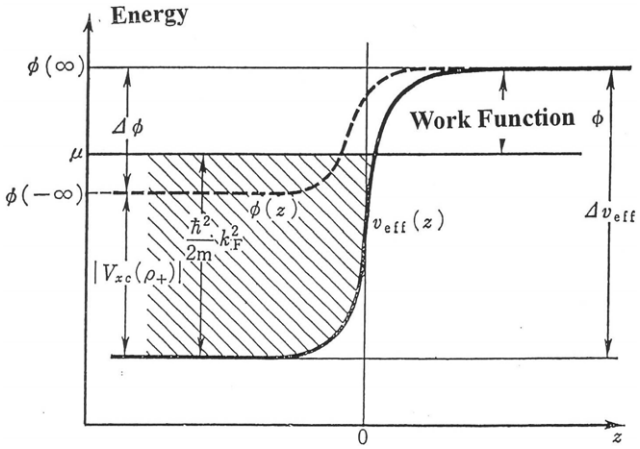

Figure 3. Potential energy diagram for defining the work function (after [19]).

of this work is that they have made clear what part of atomic structures contributes most to the field electron emission.

Watanabe claims that the Fowler–Nordheim equation is not appropriate for the field emission from nano-structures for the following reasons: (1) the electron emitting surface has a complicated three-dimensional structure in the case of CNTs, (2) electronic structures cannot be described based on the free electron approximation due to covalent bonds and strong electron–electron interactions and (3) the ease of electron emission cannot be uniquely determined by the work function but depends on the electron orbital contributing to the electron emission.

3. Work function

3.1. Work function—definition

The work function was classically defined as the amount of energy to bring an electron in the solid to a distance far away from the surface. According to this definition, the work function corresponds to the ionization potential of an atom in the solid, and is a bulk property independent of crystal planes. As is well known the work function does depend on surface crystal planes; the definition has to be modified in such a way that it is the energy to bring an electron in the solid to a distance that is much greater than the lattice size but much shorter than the crystal grain size.

In field emission we often encounter the work function on an atomic scale, although it has never been defined before. Here, the distance to bring an electron out of solid should be comparable to the lattice size. Below, the work function will be described that is widely accepted [19].

As shown in figure 3, electrons in the solid are confined in a potential well whose depth Δv_{eff} is the sum of the cohesive force potential $|V_{xc}(\rho^+)|$ and the electrostatic force potential $\Delta\phi$. The former is a bulk property that arises from exchange and correlation interactions among electrons in the solid, while the latter is a surface property that depends on surface atomic structures.

Electrons in the solid are filled in the potential well following their wave number in order until the Fermi wave number k_{F} is reached. Thus, the electron filling is completed when the electron with the energy $(\hbar^2/2m)k_{\text{F}}^2$ is filled in place.

The work function is then defined as

$$\phi = \Delta v_{\text{eff}} - \frac{\hbar^2}{2m} k_{\text{F}}^2. \tag{8}$$

The origin of the electrostatic force is the spill-out of electrons in the solid to vacuum. Spill-out electrons and positive charge left behind in the solid build up an electric dipole field that then suppresses electrons coming out of solid. As spill-out electrons smear out the space outside ion cores, the surface averaged spill-out electron density should vary with the surface atom concentration. Closely packed surfaces having less smearing action feel greater electrostatic force than loosely packed surfaces. This creates the dependence of the work function on crystal planes.

The theory of work functions based on first principles utilizing the density functional theory (DFT) was initiated by Lang and Kohn [20] assuming a jellium surface, where electrons and ion cores are uniformly distributed. Recent theories incorporating precisely the atomic structure of the surface predict the work functions of most of the single elements [21, 22].

In the following, phenomenological relations for the work function will be presented, which will then be followed by more precise recent theories as briefly described above.

3.2. Work function based on phenomenological relations

3.2.1. Work function of single elements. The work functions of single elements are plotted with their electronegativities and are shown in figure 4 [23]. We find that the work function does not depend on their crystal structures but depends linearly on the electronegativity. This is called the Gordy and Thomas relation [24].

The electronegativity χ was originally introduced by Pauling as a parameter with which bond energies of binary compounds were correlated. It has, however, a physical meaning as the electrostatic potential energy that a valence electron at the single bond length r feels from the unshielded charge Z_{eff} of the ion core:

$$\chi = \frac{eZ_{\text{eff}}}{r}. \tag{9}$$

The following phenomenological equation was derived by Gordy [25]:

$$\chi = \frac{0.31(n+1)}{r} + 0.50 \text{ (Pauling)}, \tag{10}$$

where r is in ångstroms.

The equation satisfies all elements except for noble metal elements, Cu, Ag and Au. The reason is that core electrons rather than filled valence electrons are responsible for the chemical bond in the case of noble metal elements [25].

According to the Richardson equation (1), the emission current density of thermionic emission materials is determined by the work function ϕ and the operating temperature T. Low work function and high operating temperature are, therefore, desirable to obtain a high current density, and thus the figure of merit of thermionic emission materials becomes ϕ/T_{m}, where T_{m} is the material's melting temperature. Among all single elements, a refractory metal element such as W is chosen as the best material. Although the work function is rather large, high temperature operation provides satisfactory high current density.

3.2.2. Work function of binary compounds AB. Although experimental data are dispersed quite extensively mainly due to defects and non-stoichiometry, the work function of binary

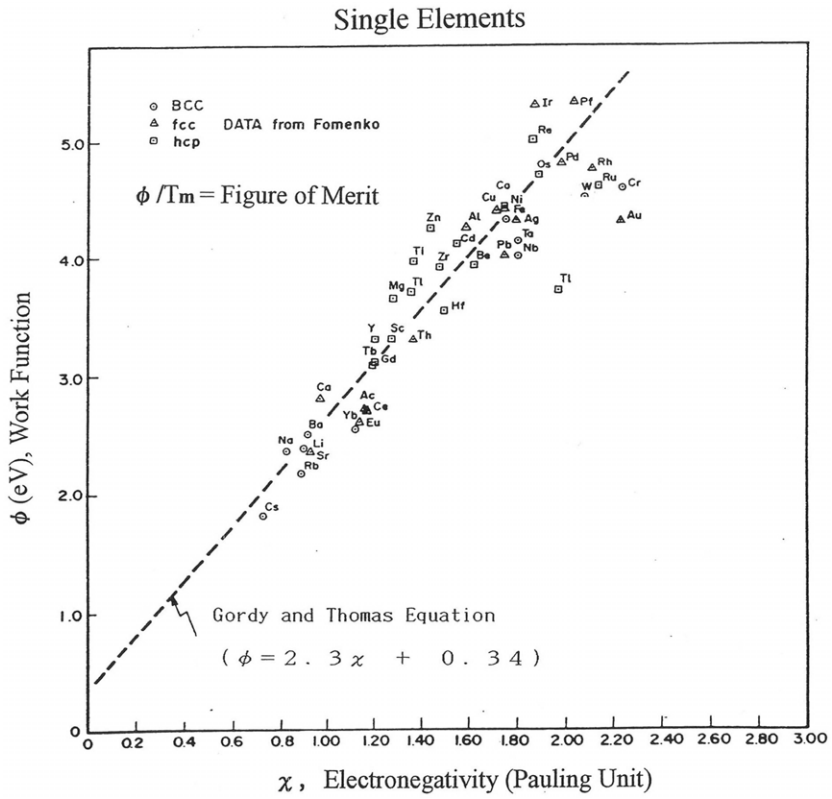

Figure 4. Relationship between the work function of single elements and their electronegativity (after [23]).

compounds AB can be correlated with the electronegativity χ_A of element A having the smaller electronegativity [23]. Here again, the Gordy–Thomas relationship holds, meaning that the work function of binary compounds is primarily determined by one of the component elements. In order to make clear the role of the second element B in the work function of binary compounds, a relationship is applied that was derived by Wilmshurst [26] for diatomic molecules (AB). Figure 5 shows a comparison of the calculated data with the measured data for a variety of binary compounds such as borides, oxides, carbides, nitrides and silicides. The metal film alloy data are also included in the figure. The agreement is quite reasonable despite the simplicity of the model.

When the materials selection is extended to binary compounds, the best choice among all binary compounds is LaB_6, which is widely used in the field of scientific instruments [27]. Another choice is alkali-earth oxides such as BaO, SrO and CaO, known as oxide cathodes. Although oxide cathodes mainly used as the electron source of electron tubes such as the cathode ray tube (CRT) have a low work function, the current density is limited to low because of the Joule heating of materials.

In field emission, W has long been chosen as a high brightness electron source for scientific instruments such as electron microscopes. Refractory metal carbides, especially their single crystals, are also used for similar purposes. Thin films of HfC have been applied to Si-FEAs (field emitter arrays) [28].

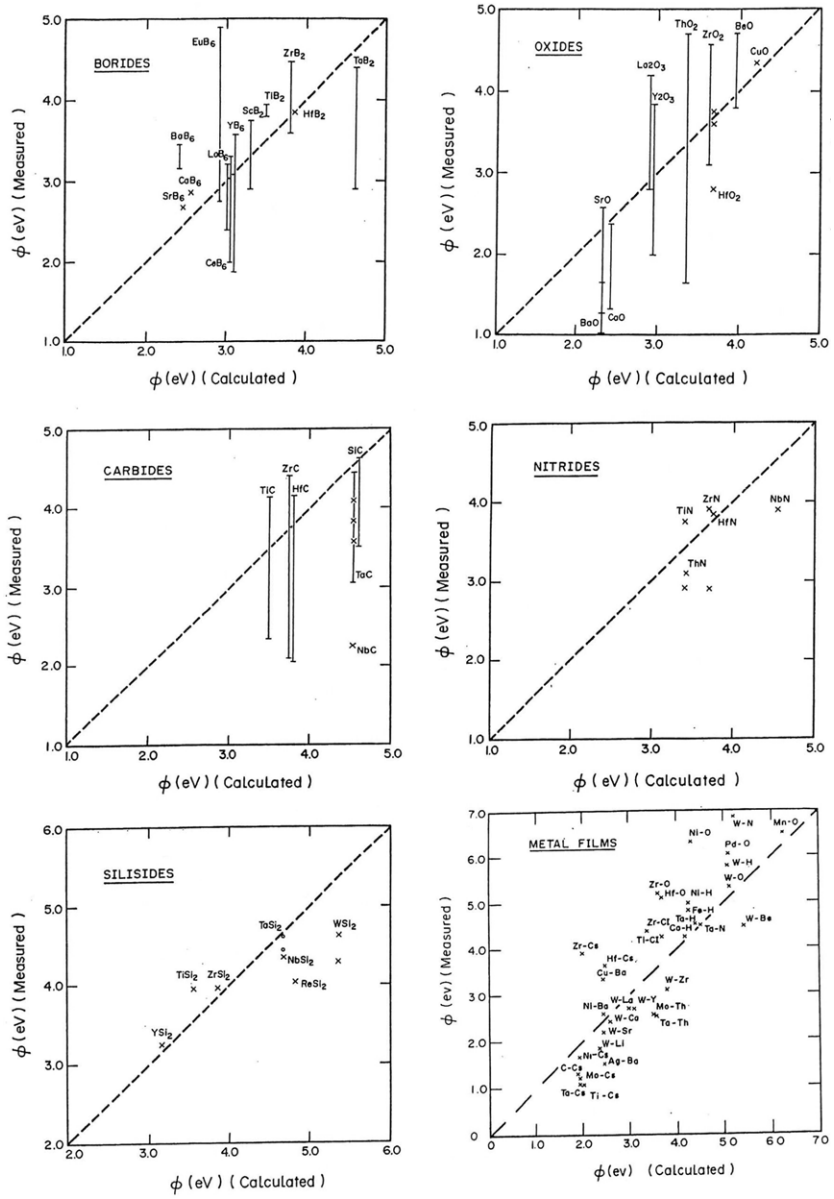

Figure 5. Comparison between the calculated (abscissa) and the measured (ordinate) of binary compounds and alloys (after [23]).

3.2.3. Work function change due to adsorption of atoms and molecules. When the surfaces of solid materials are exposed to air or vacuum, the work function is subjected to modification by the adsorption of gas atoms and molecules coming from the environment. The modification depends on surface conditions such as the surface temperature and previous surface treatments.

When an atom adsorbs on a clean surface a potential builds up on the surface, which either reduces or increases the work function of the substrate. According to the Gurney model [29] that has long been believed to be appropriate, when an alkali atom approaches a clean surface

the energy level of the alkali atom broadens and shifts upwards above the Fermi energy of the substrate metal surface. As a result, the broadened atomic energy band is partially filled with electrons from the metal substrate to make the atom a positive ion. In contrast to this model Ishida claims, based on his first principles calculation, that the adsorbed atom forms a covalent bond and makes the atom polarized [30].

In both cases an electric dipole field is built at the adsorption site, which modifies the work function of the substrate in the following manner.

The surface potential ΔV created by a dipole moment $P = qd$ with the density σ is given by

$$\Delta V = \frac{Q}{C}, \tag{11}$$

where charge Q is the total charge given by the sum of the elemental charge q of the dipole and its concentration σ as $Q = q\sigma$ and C is the electrostatic capacitance.

Assuming a parallel plate configuration with the area S and the dipole length d, the capacitance is given by

$$C = \varepsilon_0 \frac{S}{d}. \tag{12}$$

Then, (11) is expressed as

$$\Delta V = \frac{qd\sigma}{\varepsilon_0} = \frac{P\sigma}{\varepsilon_0}. \tag{13}$$

Here, the polarity of ΔV can take either a positive or a negative sign depending on the polarity of adsorbed ions. The change in the work function by atom adsorption is, thus, given by

$$\Delta\phi = -\Delta V. \tag{14}$$

Experimental verification of (13). The maximum change in the surface potential of W surfaces divided by the ionic radius of adsorbed species is plotted in figure 6 with the electronegativity χ_a (not in Pauling units) of adsorbed species [31]. A beautiful linear relationship can be recognized, the reason for which can be understood as follows.

From (13), $\Delta V/d$ is expressed as a function of the difference in electronegativity between adsorbate χ_a and substrate χ_s as

$$\frac{\Delta V}{d} \propto Q \cong \chi_a - \chi_s. \tag{15}$$

When we take the ionic radius of the adsorbed specie as d, then figure 6 becomes the experimental verification of (13). Interestingly enough, we find from figure 6 that the electronegativity should depend on the crystal plane.

The case of high adsorbate coverage. According to (13) the surface potential varies linearly with the adsorbate surface concentration. The relation, however, breaks down as the surface coverage increases and depolarization starts as a result of dipole–dipole interaction, in which case the relation (13) has to be modified as

$$\Delta V = \frac{\Delta V_0}{1 + 9\alpha\theta^{3/2}/4\pi\varepsilon_0 a^3}, \tag{16}$$

where ΔV_0 is the surface potential without dipole–dipole interaction, θ the adsorbate surface coverage and a the lattice constant of a square lattice used in this expression. The final expression is given by

$$\Delta V = \frac{P_0\theta/(a^2\varepsilon_0)}{1 + 9\alpha\theta^{3/2}/4\pi\varepsilon_0 a^3}. \tag{17}$$

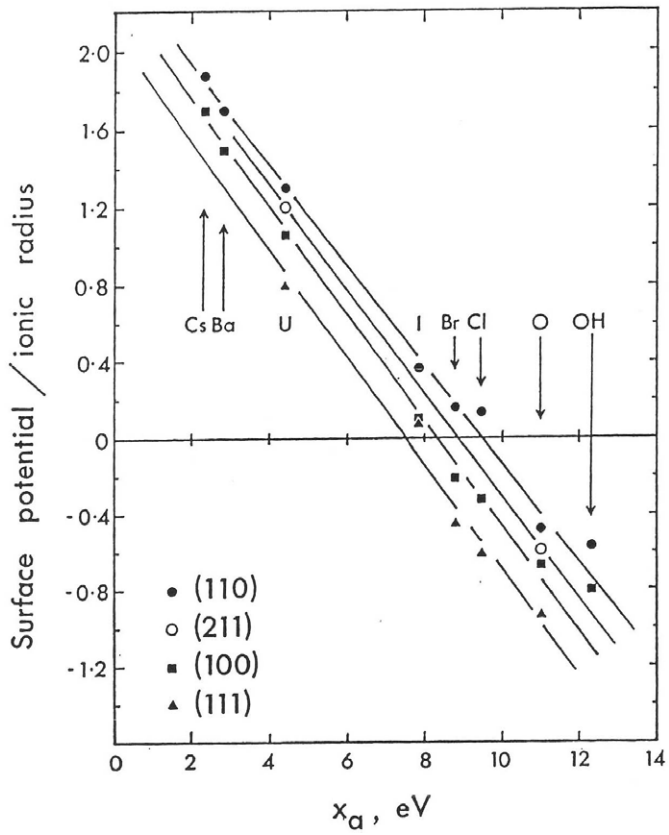

Figure 6. Surface potential induced on four W single crystal planes with different orientations by adsorption of various atoms, molecules and radicals (after [31]). (The surface potential divided by the ionic radius of adsorbates is plotted with the electronegativiy of adsorbates.)

This equation indicates that the surface potential is not a linear function of the adsorbate surface coverage but may experience either a maximum or a minimum at certain coverage.

3.2.4. Work function of surface monolayer cathode. When a low work function surface is supported by a substrate with a high melting temperature, we will find a material carrying the best figure of merit as a thermionic emission source. Thoriated tungsten is believed to be the first monolayer type thermionic cathode in which Th (or ThO) is supplied from a W body to reduce the work function from 4.5 to 2.6 eV. Commercial products on this track were dispenser cathodes developed at Philips Research Laboratories during the period between the 1950s and the 1960s [32–34]. A component element, Ba, of the low work function (about 2.0 eV) Ba–O monolayer is continuously supplied from the substrate W body in this cathode. Dispenser cathodes replace oxide cathodes in the field where a high current density heavy duty use is required.

A similar idea was applied for field emission materials. Swanson *et al* developed an innovative field emission material, in which a Zr–O monolayer covers a W substrate to selectively reduce the work function of the (100) plane as low as 2.5 eV [35]. The layer is replenished continuously from the W substrate even under heavy ion bombardment. This

cathode is widely used in scientific instruments as well as in electronics device fabrication machines utilizing electron beams that require high current density and high current stability.

3.3. Work function on the atomic scale

Although the concept of the work function on the atomic scale is not yet widely accepted, it is important to understand the field emission capability of materials, in which electron emission sites are often atomic in size. As already mentioned previously, the macroscopic work function is defined based on the energy band structures. However, it becomes more and more important in nanotechnology to get into the details of electron orbitals at the emission site rather than the over all band structures. In the following, we will describe the definition of the work function on the atomic scale and, then, try to correlate it with the conventional macroscopic work function.

3.3.1. Work function on the atomic scale, definition. The importance of the 'local work function' was already addressed by Wandelt in the plenary talk at the 1st International Vacuum Electron Source Conference (IVESC'96) held in Eindhoven, The Netherlands, in 1996. In the talk he introduced a novel way of measuring the local work function, photoemission of adsorbed xenon (PAX) [36]. In this paper, however, we have applied another way of obtaining the work function on the atomic scale instead of PAX because of its experimental easiness and the better spatial resolution expected.

Among others, one of the best ways to measure the electronic structure of solid surfaces is scanning tunnelling microscopy (STM). The tunnelling current between an STM probe tip and a sample separated by a distance z is expressed by the following relation [37], which has been experimentally verified [38]:

$$I_{\mathrm{T}} \propto \exp(-2\kappa z). \tag{18}$$

Here, 2κ is the decay constant and is expressed by utilizing the tunnelling barrier height Φ as

$$2\kappa = 2\frac{(2m\Phi)^{1/2}}{\hbar}. \tag{19}$$

From (18) and (19) Φ is given by

$$\Phi = \frac{\hbar^2}{8m}\left(\frac{\mathrm{d}\ln I_{\mathrm{T}}}{\mathrm{d}z}\right)^2. \tag{20}$$

From (20) the tunnelling barrier height can be obtained from the derivative of the tunnelling current with respect to the separation. For the one-dimensional scheme, the tunnelling barrier height is given by the arithmetic mean work function of the STM tip and the sample as

$$\Phi = \frac{\Phi_{\mathrm{T}} + \Phi_{\mathrm{S}}}{2}. \tag{21}$$

Hence, if Φ_{T} is known, then the sample's work function Φ_{S} can be logically obtained from barrier height measurements. From now on, we will name the tunnelling barrier height the 'local barrier height' or the LBH because it conveys the local information on the atomic scale. The values on the atomic scale will be denoted by capital letters, and the macroscopic values by small letters. Since no one knows the exact value of Φ_{T}, the work function of the sample on the atomic scale also remains uncertain. Later we will discuss the change in the work function on the atomic scale rather than the absolute value. The change in the work function on the atomic scale is well correlated with the change in the macroscopic work function.

$$\Phi = \frac{\hbar^2}{8m}\left(\frac{d\ln I_T}{dZ}\right)^2$$

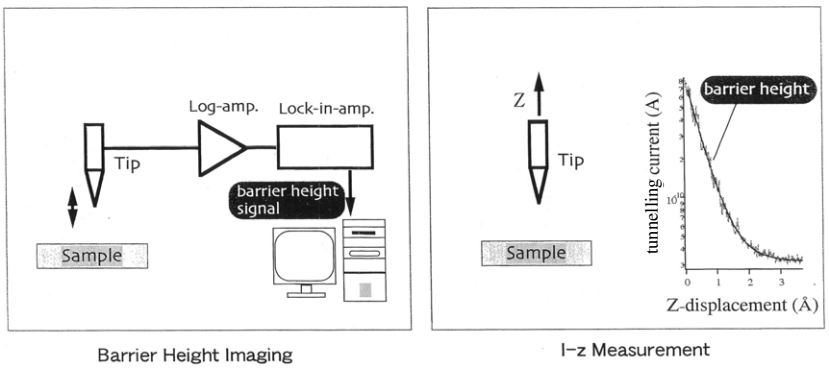

Figure 7. Two methods for local barrier height measurements (LBH). Left: high speed method for simultaneously obtaining LBH and STM images. Right: quantitative measurement method (I–z method).

3.3.2. Work function measurements on the atomic scale. Figure 7 shows the outline of two methods of LBH measurements. As shown in the left figure, under the constant current mode operation in STM, the STM probe tip is forced to oscillate at a frequency much greater than the feedback frequency of the STM operation. The obtained tunnelling current is first log-amplified and then fed to a lock-in amplifier to take a derivative with respect to the tip–sample separation. A good point of this technique is that both LBH and STM images can be obtained simultaneously. A drawback, however, is the difficulty in obtaining reliable quantitative LBH values because of the non-linearity of PZT motion, the effect of stray capacitance and so on. To make more reliable and reproducible LBH measurements, as shown in the right-hand figure, the STM tip is slowly ($\cong 1\,\mathrm{nm\,s^{-1}}$) lifted from a position very close to the sample and the tunnelling current is recorded with the displacement [38–40]. This technique is called the I–z method for LBH measurements.

3.3.3. Relationship between macroscopic and microscopic work functions. As shown in figure 8, the work function measured by the Kelvin method of a Pt(111) surface decreases by depositing Cs on the surface, and superstructures appear depending on the Cs coverage [41]. The work function attains the minimum at the 0.25 monolayer of Cs coverage, and a thermally stable (2×2) superstructure is recognized. A further increase in the Cs coverage increases the work function a little bit, and the superstructure is converted into a commensurate phase $(\sqrt{3} \times \sqrt{3})R30$ and then to an incommensurate $(\sqrt{3} \times \sqrt{3})$ phase as the coverage increases. As these phases, however, are not thermally stable, they transform into the more stable (2×2) phase at room temperature.

STM and LBH images. Figure 9 shows STM and LBH images [39], which are obtained at the Cs coverage of 2.5% corresponding to the 2 eV reduction in the work function. The dark areas seen in the STM image in the background of Pt lattice atom images correspond to adsorbed positions of the cluster of a few Cs atoms. Here, the number of electrons is deficient because some electrons are transferred to the substrate. The LBH is found to be low at Cs positions.

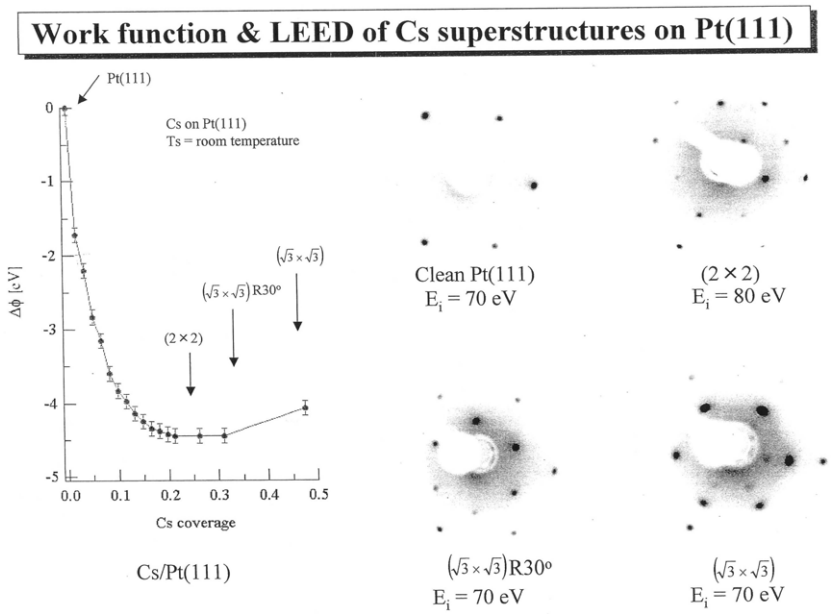

Figure 8. Change in the work function of Pt(111) by Cs adsorption and the corresponding LEED images (after [41]).

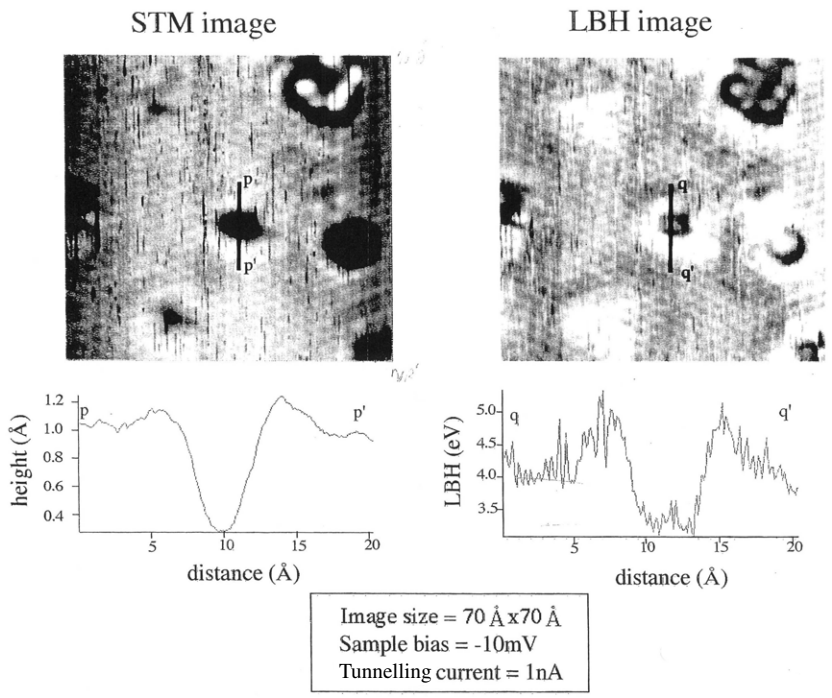

Figure 9. STM and LBH images of the Pt(111) surface covered by 0.025 monolayer Cs and line-scans of both images (after [39]).

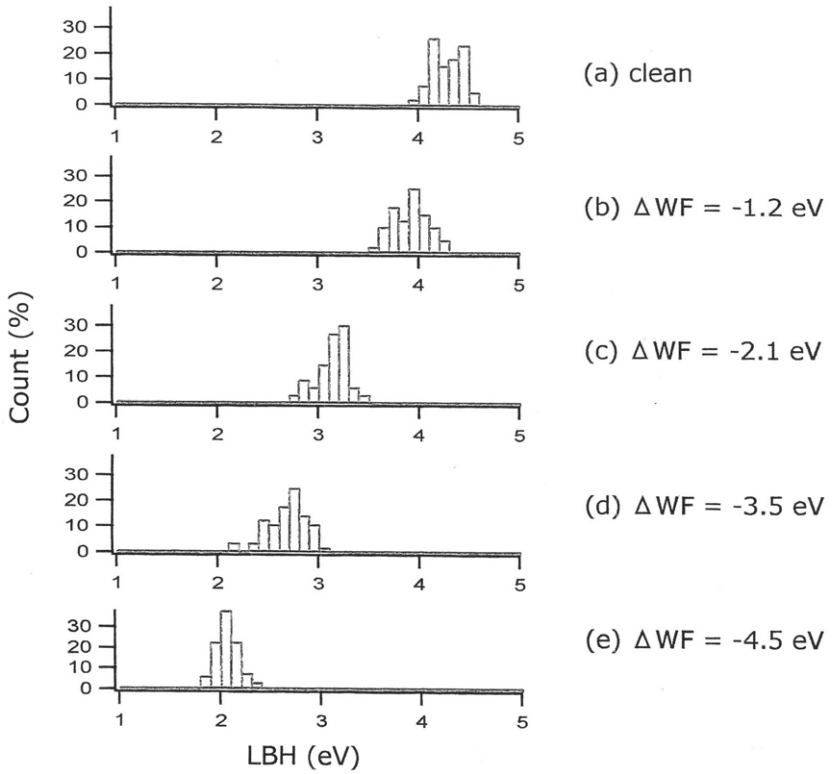

Figure 10. Histogram of 50 LBHs measured on the Pt(111) surface covered with various surface coverage of Cs (after [40]). (The change in macroscopic work function on the right represents the Cs coverage estimated from figure 8.)

A line-scan is made to qualitatively measure the size of image corrugations. At the bottom of the STM line-scan the depth can be measured to be about 0.05 nm, which indicates the electron density deficiency. On the other hand, outside the dip periphery, an excess electron density can be recognized that compensates deficient electrons in the dip. At the bottom of the dip the LBH is lower than the outside by 0.5–1.0 eV.

LBH histograms of Cs adsorbed on Pt(111). Histograms of LBHs obtained by the I–z method at 50 points each in an LBH image are taken under various Cs coverage. The result is shown in figure 10, where the change in the macroscopic work function represents the Cs coverage. If the influence of the Cs adsorption is 'local', limited only to nearest neighbours, then we would expect to observe two distinct peaks in the histogram, one from Cs and the other from bare Pt. The figure, however, shows that it is not true but that the influence of Cs adsorption extends over many lattice points. This is a very important finding that has never been reported before. This long range interaction also influences surface chemical reactions incorporating a very small number of atoms on the surface and has been experimentally verified recently by supersonic molecular beam experiments [41, 42].

Another important finding can be seen in figure 11 when the change in the LBH is plotted versus the change in the macroscopic work function measured by the Kelvin method. From the figure we obtain the following relation that relates the ensemble average of the LBH, $\langle \Delta\Phi \rangle$

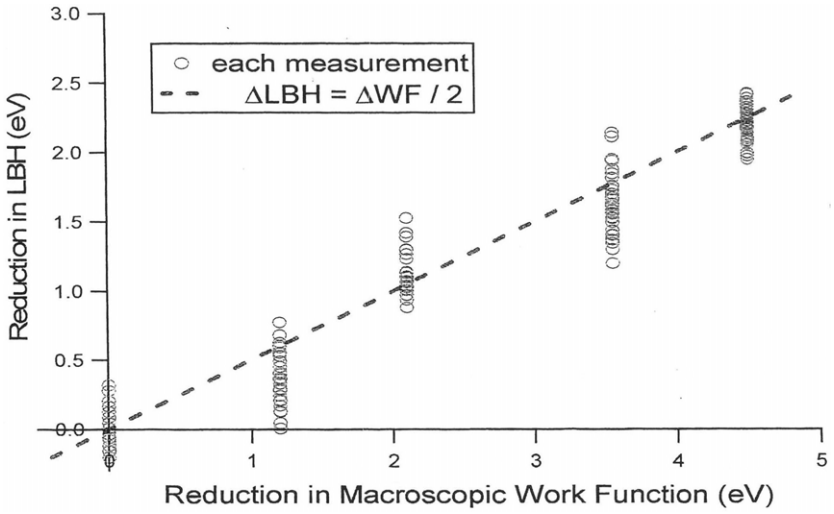

Figure 11. Relationship between the changes in LBH and macroscopic work function of the Pt(111) surface covered with Cs at various coverage (after [40]).

to the change in the macroscopic work function, $\Delta\phi_S$, as

$$\langle \Delta\Phi \rangle = \frac{\Delta\phi_S}{2}. \tag{22}$$

If the work function of the tip surface Φ_T does not change during measurements and the one-dimensional tunnelling barrier height is accepted, then the following relation will hold:

$$\Delta\phi_S = \langle \Delta\Phi_S \rangle. \tag{23}$$

The change in the macroscopic work function equals the ensemble average of the change in the work function on the atomic scale. This is another important finding that correlates microscopic and macroscopic work functions.

3.4. Theoretical aspect of work function

A strict theory of the work function was reported for the first time by Lang and Kohn in the 1970s [20]. By applying the DFT they obtained from first principles the work function of simple single elements. Later the theory was improved in the 1990s so as to be applicable to more complicated single elements such as transition metal and noble metal elements [21, 22]. The theory, nowadays, is also applied to the work function of metal-carbides [43, 44]. The change in the work function by atom adsorption was calculated based on first principles, for BaO on a tungsten substrate of dispenser cathodes [45], BaO on W(100) [46], Na and K on Rh(111) [47] and so on.

3.4.1. Work function of single elements (theory). In the model developed by Lang and Kohn, a uniform distribution is assumed of ion cores and electrons in the solid [20]. In this model, often called the jellium model, the only variable is the electron density (or ion density) in the solid. In the later model [48], called the lattice model, they introduced ion core positions as a perturbation, thereby including the smearing effect [49]. Their model reproduces the work function of simple single elements with s and p orbitals well enough, but it fails when applied

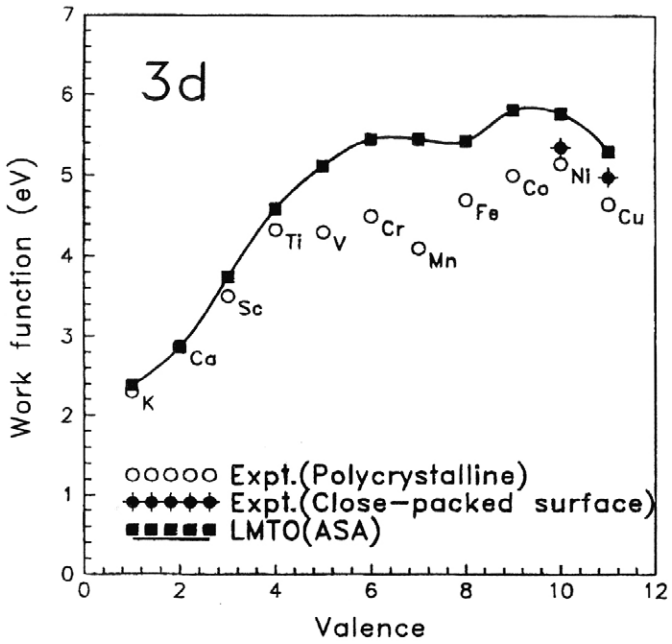

Figure 12. Comparison of the measured work function of 3d metal elements with the calculation based on the LMTO-ASA model (after [21]).

to more complicated elements such as transition metal and noble metal elements where the d electron orbital plays a dominant role.

Stricter work function calculations were made by applying self-consistently the linear muffin-tin orbital (LMTO) method to include exact optimum positions of ion cores. Skriver and Rosengaard computed the work function of 3d, 4d and 5d transition metal and noble metal elements in addition to alkali and alkali-earth metal elements [21]. Methefessel *et al* did a similar but a more exact full potential-LMTO SLAB calculation to determine the work function of 4d series elements [22]. Skriver and Rosengaard formulated the work function with the number of valence electrons (d and s orbital electrons) and compared it with the experimental results [50] as shown in figure 12 for 3d elements. As the calculation was made based on closely packed surfaces only, while experimental data include various crystal planes, calculated values were overestimated in some cases. Also included in the figure are the experimental data obtained from closely packed surfaces, which agree better with the theory. It is found that the work function is closely correlated with the number of valence electrons as in the case of phenomenological relations.

3.4.2. Work function of binary compounds (theory). The work function of binary compounds can be calculated just as in the case of single elements. As an extension of the work by Skriver and Rosengaard, Hugosson *et al* computed the work function of (3d to 5d) transition metal carbides based on the LMTO method [43]. They found that the work function of 3d metal element carbides is a little bit greater than that of single metal elements, while the opposite case is true for 5d metal carbides. In any case, the work functions of carbides do not differ very much from those of respective single metal elements, just as in the case of the phenomenological relationship. Kobayashi did similar work many years ahead of Hugosson *et al* although the

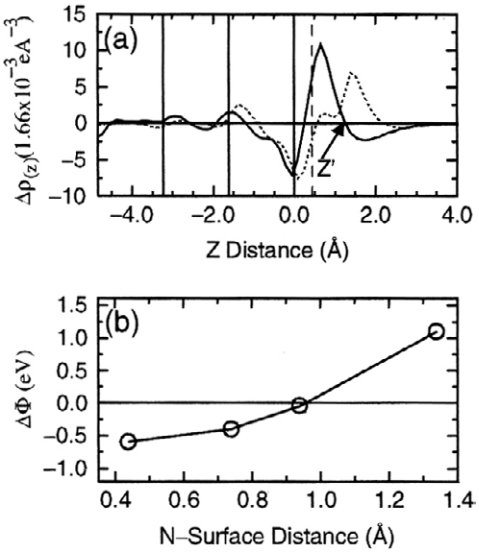

Figure 13. Dependence of the distance from the surface of the change in charge density before and after N adsorption (*a*) and the dependence of the work function change on N to the surface distance (*b*) (after [52]). (Solid and dotted curves in (*a*) represent the cases when N adsorbs at 0.044 nm (equilibrium position) and 0.134 nm from the surface, respectively.)

calculated work function was limited to a small number of transition metal carbides [44]. In his calculation, it was predicted that the surface carbon atom was positioned up towards the vacuum side from the equilibrium position in the solid. This modified structure was later verified by the LEED experiment [51].

3.4.3. Work function of a monolayer (theory). Based on the DFT, Xiao *et al* concluded that the adsorption is on the most stable hcp hollow site of Rh(111) and that Na and K transfer to the substrate 0.13 and 0.18 electrons, respectively [47]. This result supports the Gurney model. Mueller calculated the amount of charge transfer of Ba–O on a tungsten substrate in order to simulate a dispenser cathode and found that 1.5 electrons from a Ba atom are transferred to the substrate, while O forms a covalent bond with the substrate [45]. All the above results support the phenomenological discussions in section 3.2.

The next example emphasizes the importance of the strict theory of the work function [52]. From the difference in electronegativity, the adsorption of nitrogen atoms on a W surface introduces an increase in the work function. However, known as an ancient surface science anomaly, N adsorption on W(100) decreases the work function, while, as predicted, the work function increases on other planes of W [53]. This anomaly has recently been resolved by the theoretical work based on first principles [52]. The most essential point of this work is what is important is not the charge polarity of the adsorbed N but the modified distribution due to N adsorption of the electron cloud extending to vacuum.

Figure 13 describes the mechanism of how the work function of the substrate surface is modified by N adsorption. The upper figure (*a*) shows the dependence on the distance z of the electron charge density difference $\Delta\rho$ before and after N adsorption. The solid curve indicates the case for the equilibrium distance 0.044 nm of the N adsorption site as shown by a vertical dashed line, while a dotted curve is the case for N adsorption far away from the surface. At the

distance $z = 0$, at the solid–vacuum interface, $\Delta\rho$ is negative because electrons are transferred to the N atom, while it becomes positive at the N adsorption site. (The N atom is negatively charged by adsorption.) At a distance $z \cong 0.2$ nm, there is another dip in $\Delta\rho$, which is caused by the electron donation from the W 5d orbit to the N atom. As the overall change in the dipole moment as expressed by

$$\Delta\mu = \int z\Delta\rho(z)\,\mathrm{d}z \tag{24}$$

is strongly influenced by $\Delta\rho$ at a large distance such as at $z \cong 0.2$ nm, the resultant work function change becomes negative as shown in figure 13(*b*). This shows the z dependence of the change in the work function due to N adsorption. If N were adsorbed at a distance away from the surface or the solid curve were terminated at the distance Z, as shown in figure 13(*a*), then $\Delta\rho$ would not be negative at the distance away from the surface. From the result described above, the work function is determined not by the polarity of the adsorbed N but by the modified distribution of the electron cloud extending to vacuum. This has been made possible only by calculating the exact location of the N adsorption site.

4. Historical review of thermionic emission materials

4.1. Tungsten and thoriated tungsten cathodes

Probably, W is the most ancient material in the history of thermionic electron emission materials. Although the work function is rather large, high temperature operation provides a high current density such as 1 A cm^{-2}. The W electron source was developed by Langmuir *et al* and commercialized initially as a light source of electric bulbs at the General Electric Company in the 1900s. Since the invention of the electron microscope in the 1930s, a W hairpin was installed as an electron source, until it was replaced by a LaB_6 thermionic electron emission source in the 1960s and then by a W field emission electron source in the 1970s. One of the advantages of the W electron source, hereafter called 'cathode', is that it does not require good vacuum because high temperature operation prevents gas adsorption on the cathode surface. However, high temperature operation shortens the life due to the material loss by evaporation and limits the maximum operation temperature and hence the current density, $\leqslant$1 A cm^{-2}.

The thermionic emission current density of the W cathode was found to be enormously improved by adding a small amount (0.5–1.5%) of ThO_2 (thoria) to the W body. By heating at 2700 K for decomposition followed by annealing at 2100–200 K, Th atoms diffuse and build a monolayer on a W surface, which then reduces the work function of W from about 4.5 down to 2.6 eV. This cathode, well known as a thoriated W cathode, provides the current density $\cong$4 A cm^{-2} at the operation temperature above 2000 K [54, 55]. The work function is about 2.6 eV, which is smaller than the work functions of both Th (about 3.3 eV) and W. This cathode is probably the oldest monolayer cathode ever developed. Although the cathode was extensively applied in various fields in the past, its use has however been limited recently, because ThO_2 is a radioactive material under rigorous control. To replace thoriated W cathodes, a Mo–La_2O_3 cathode has recently been developed [56], in which a monolayer of La–O contributes to maintain the low work function of the cathode.

4.2. Lanthanum hexabaride (LaB_6) cathodes

Pressed LaB_6. Among all binary compounds ever fabricated, LaB_6 shows the best figure of merit as a thermionic emission material. LaB_6 is a good electric conductor, as good as Pb, with a high melting temperature and a peculiar structure. A La atom is contained in the structure

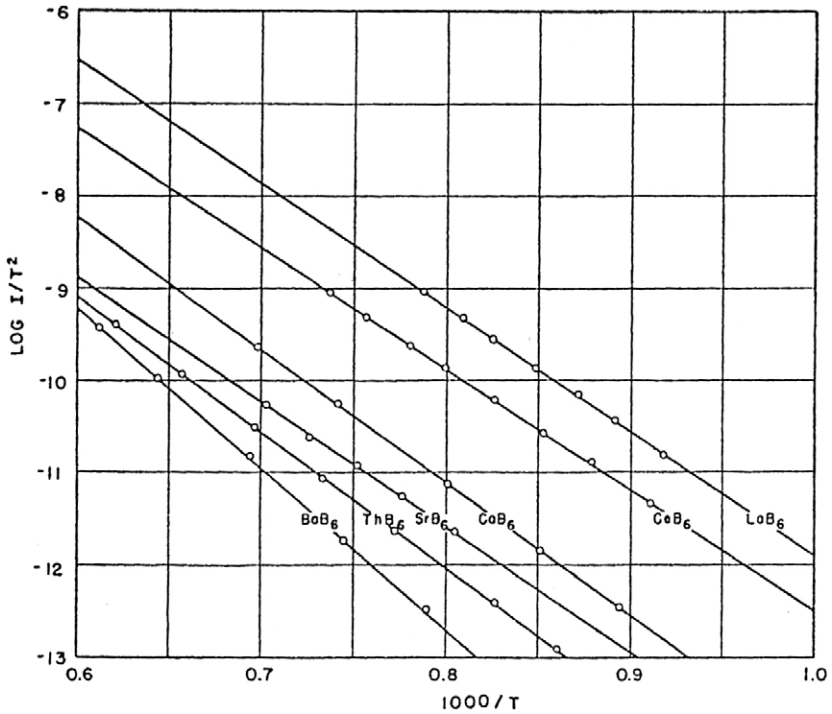

Figure 14. Emission capability of metal hexaborides (after [27]).

(CsCl type structure) composed of octahedral boron cages each located at all corners. The lattice constant of LaB_6 is $a_0 = 0.4145$ nm, which does not depend too much on metal atom species and their sizes contained in the boron mesh [57].

After their discovery in the 1930s [57] only a very few researchers with their strong curiosity paid attention to the series of metal borides, until Lafferty of GE Co. reported their excellent electron emission capability in the early 1950s [27], 20 years after the first report. Twenty years after Lafferty, in the late 1960s, quite a lot of people rushed to investigate the material when Broers of IBM experimentally proved that the spatial resolution of electron microscopes had been improved by many orders of magnitude when applying LaB_6 as an electron source [58].

Lafferty fabricated various pressed hexaborides to compare their emission capabilities, which included borides of alkali-earth metal atoms and rare-earth metal atoms [27]. As shown in figure 14, LaB_6 shows the best emission performance among others. The order of good increasing emission capability is $LaB_6 > CeB_6 > CaB_6 > SrB_6 > ThB_6 > BaB_6$. In order to maintain the high electron emission of LaB_6, the La layer must be maintained on the surface and therefore high temperature activation is mandatory for good electron emission. The loss of La atoms on the surface by ion bombardment results in the deterioration of the emission capability [27].

Single crystal LaB_6. As the demand for scientific instruments utilizing LaB_6 cathodes started to increase in the early 1970s, scientists started to request a good quality cathode that would provide high brightness, high emission current stability and a long life [59]. On their demand single crystal LaB_6 was fabricated either by the floating-zone (FZ) method or by the Al flux

method, and the dependence of the work function on crystal structures was examined [60–63]. Among various crystal planes the (100) plane was found to provide the lowest work function, indicating that the surface with a high La concentration provides a low work function.

Operation principle of LaB_6 cathode. One of the factors determining the electron emission of LaB_6 is the La concentration on the surface as judged from the dependence of the emission capability on the crystal plane. Moreover, in his paper Lafferty claimed that the surface coverage of La atoms plays a key role in electron emission [27]. He believed that the work function is reduced by the surface potential induced by the dipole field formed as a result of the surface monolayer.

On the other hand, based on modern surface analyses, good electron emission is found to be realized from the LaB_6 cathode with a stoichiometric composition even under operational conditions [60,64,65]. That is, electron emission is determined by the bulk property of the LaB_6 cathode although we admit that it experiences some perturbation by adsorbed gas molecules under poor environment.

Very few papers report on the field emission from LaB_6. It is, however, found that the emission current from the (100) plane is very unstable, twice as unstable as the field emission from W [66]. This may be because the outermost La atom on the surface is so active chemically that the current fluctuation is easily induced by ambient gas adsorption.

4.3. Oxide cathodes

The oxide cathode is probably the second oldest thermionic electron source next to the W cathode. It was discovered in 1904 by Wehnelt and since then has been extensively used in the field of electron tubes such as the CRT and will still be used in the future. No other cathode can and will be able to catch up with its high reliability and stability as well as the low work function and the low production cost.

A drawback is its low electric conductance compared with metals, which limits the maximum current density obtainable due to Joule heating of the cathode material. It is well known that overheating causes sintering, melting and destruction of the oxide material.

Under the ordinary operation of CRTs, the current load averaged over the whole cathode surface is designed below $0.5\,\mathrm{A\,cm^{-2}}$ (sometimes $1.0\,\mathrm{A\,cm^{-2}}$). Assuming a Gaussian distribution of the current density over the cathode surface by taking into account field penetration from the grid aperture, the peak current density is about 2.5 times [67] the average $1.25\,\mathrm{A\,cm^{-2}}$, while modern display tubes such as high definition tubes require a maximum current density of $10\,\mathrm{A\,cm^{-2}}$, that is, eight times (or four times) greater than the current density that the oxide cathode can stand.

4.3.1. Oxide cathode structure. A typical oxide cathode consists of a Ni sleeve about 1 mm in diameter on top of which electron emissive materials are spray coated 10–80 μm in thickness. For vacuum microwave devices, the coating is much thicker and the cathode size is much larger than in the case of CRTs. The cathode is heated indirectly by a heater inserted in the Ni sleeve. The electron emissive material is a mixture of Ba and Sr carbonates and 6% mole of Ca carbonate, which are decomposed into oxides by heating at 950 °C in vacuum after sealing off. The oxide grains are columnar in shape, are about 1 μm in diameter and are several micrometres long. The porosity of the oxide layer is very high, of the order of 75%.

The electron emission mechanism of oxide cathodes is illustrated in figure 15 [68]. As an activator, an extremely small amount (on the order of ppm) of impurity elements such as Mg and Si is added in a very pure Ni base sleeve. Less common activators are W and Zr, that are

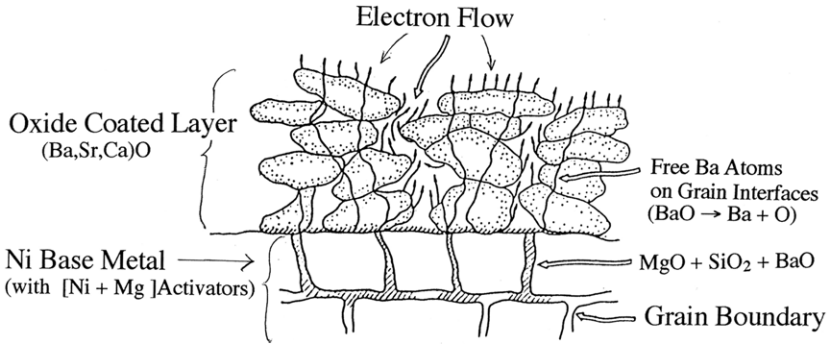

Figure 15. Schematic image of electron emission mechanism of oxide cathodes (after [68]).

included in Ni up to the solid solution limit [69]. Oxide materials, mainly BaO, react with the activator to reduce BaO and release free Ba atoms (or to create O vacancies), which migrate on oxide grains and then evaporate into vacuum. The activated cathode surface has a high capability of electron emission. The electrons emitted from the grains either migrate on and in the grain surface (grain conduction) or flow through pores between grains (pore conduction) by producing secondary electrons on the way [70]. Reaction products such as MgO and SiO_2 or Ba-silicate thus formed during reduction processes are left at metal grain boundaries, at the boundary between oxide and base metal or are left in oxide grains. When Zr and/or W are used as activators, reaction products stay only at the oxide–base metal interface [69].

Activators. Activators are categorized into three groups based on the activation power, the power for Ba production [71]. Mg, Zr, Al, Si, Th, Be, Hf, Sc, Y, Sm, Nd, Pr, La and U belong to the first group with the strongest activation power capable of producing a Ba vapour pressure as high as metal Ba. Members of the second group having an intermediate activation power are Ce, Ti, C, Ta, Mn, B, W, Cr, Mo, Ga, Zn, V and Fe. The third group has the least activation power and can no longer be called activators. The vapour pressure they produce is as low as that from BaO. The group includes Ni, Co, Cu, Au, Ag, Pt, Cd, Sb, Bi, Ir, Tl, Pd, Ru, Rh and Os.

The Ba vapour pressure, P_{Ba}, proportional to the Ba production rate, strongly depends on the activator and is given by Rittner [71] as

$$\log P_{\mathrm{Ba}} = -\frac{A}{T} + B, \tag{25}$$

where A and B are constants specific to the type of activator.

Another important aspect of the activators is the diffusion speed of the activators along the Ni grain boundaries. Fast activators are Zr, Mg and C.

Besides the reaction of the activators with BaO, the decomposition of BaO is also possible by thermal dissociation and electrolysis during activation and current drawing.

4.3.2. Work function of oxide cathodes. There are several oxide cathode materials: (1) BaO, (2) a binary solid solution of equal moles of BaO and SrO and (3) a triple solid solution of equal moles of BaO and SrO with 5–6% mole of CaO. It is believed that they have been developed successively in order to reduce the work function, to reduce the Ba evaporation rate, to suppress sintering and so on. Measured work functions of oxides are reported in [72]. The following are the results measured by the Kelvin method of a series of oxides spray coated

on a Ni substrate base metal [73]. The reference electrode used in the Kelvin method is a W ribbon heated at 2300–2500 K, the work function of which is taken to be 4.5 eV. It is surprising that although the oxide cathode is known as a semiconductor the obtained work function fits well with the work function derived from the Richardson equation (1) with

$$\phi = \phi_0 + \alpha T \tag{26}$$

and

$$A = 120.4\,\mathrm{A\,cm^{-2}\,K^{-1}}. \tag{27}$$

Obtained work functions are as follows:

$$\text{BaO: } \phi\ (\text{eV}) = (1.6 \pm 0.08) + (5 \pm 1) \times 10^{-4}\,T, \tag{28}$$

$$\text{(Ba, Sr)O: } \phi\ (\text{eV}) = (1.2 \pm 0.05) + (5 \pm 1) \times 10^{-4}\,T, \tag{29}$$

$$\text{(Ba, Sr, Ca)O: } \phi\ (\text{eV}) = (1.1 \pm 0.05) + (5 \pm 1) \times 10^{-4}\,T. \tag{30}$$

The above results indicate that the work function of oxide cathodes tends to decrease by adding extra alkali earth metal oxides.

In order to maintain the low work function of the cathode, a high enough concentration of Ba atoms σ has to be supplied continuously on the oxide material despite the electron emission mechanisms, either monolayer model or semiconductor model.

Under a dynamic equilibrium the following condition must be satisfied between supply and evaporation rates of Ba atoms

$$\sigma = \dot{n}\tau S, \tag{31}$$

where $\dot{n}$ is the supply rate, τ the mean residence time of Ba on the surface determining the desorption (evaporation) rate and S the sticking probability ($S \cong 1$). Based on the kinetic theory of gases, the Ba supply rate is given by

$$\dot{n} = \frac{P_{\mathrm{Ba}}}{\sqrt{2\pi mkT}}, \tag{32}$$

where P_{Ba} is the Ba vapour pressure and m the mass of a Ba atom.

The mean residence time τ is given by

$$\tau = \tau_0 \exp\left(\frac{E_{\mathrm{d}}}{kT}\right), \tag{33}$$

where E_{d} is the desorption energy of the Ba atom closely related to the binding energy of Ba to the substrate and τ_0 a constant of the order of 10^{-13} s.

If the desorption energy is assumed to be independent of the Ba surface coverage, which is usually the case under low coverage, then the Ba concentration is solely determined by the Ba vapour pressure that depends on the supply rate of activators. Therefore when the activator supply is reduced or interrupted by an interface layer, the cathode cannot maintain its low work function anymore and the cathode life soon becomes terminated. Oxide sintering that reduces the effective surface area of the cathode also leads to cathode life termination. Sintering occurs by Joule heating of the cathode material, which is often triggered by the interface layer with a high electrical resistance.

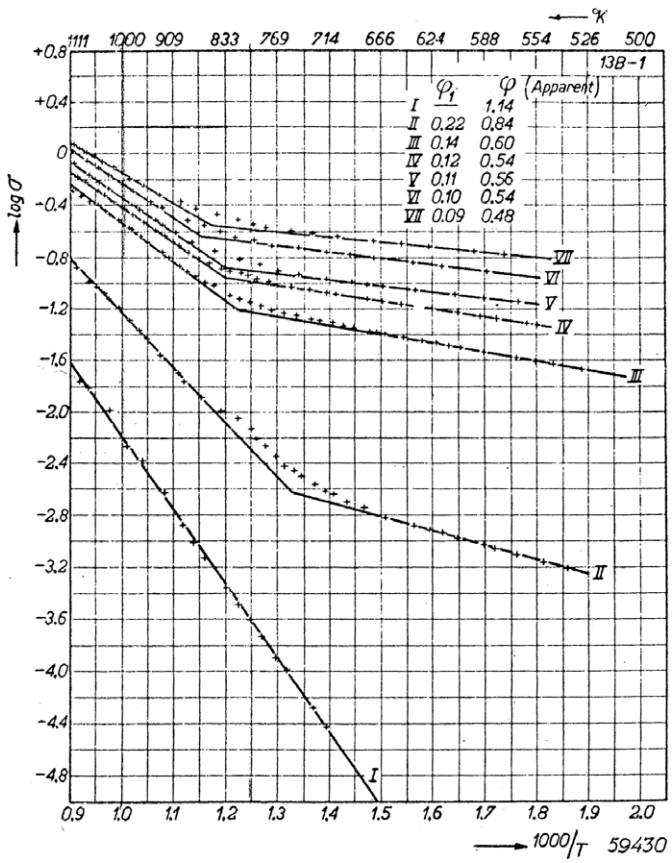

Figure 16. Temperature dependence of the electric conductivity of oxide cathodes (after [74]).

4.3.3. Electron conduction mechanism of oxide cathodes. A very unique feature of the electron conduction mechanism was discovered at the Philips Research Laboratories during the period between the late 1940s and the early 1950s [70, 74]. The operation temperature dependence of the electron conductivity is shown in figure 16 for a binary oxide (BaSrO) of 50–60% porosity coated on a Ni base metal [74]. On increasing the temperature the slope switches from low to high values, suggesting two independent conduction channels.

As the conductivity is generally given by

$$\sigma = \sigma_0 \exp\left(-\frac{\phi}{kT}\right), \tag{34}$$

the conductivity with two independent channels as in the case of figure 16 will be expressed as a sum of two parallel conduction channels as

$$\sigma = \sigma_{01} \exp\left(-\frac{\phi_1}{kT}\right) + \sigma_{02} \exp\left(-\frac{\phi_2}{kT}\right), \tag{35}$$

where ϕ_1 and ϕ_2 are the activation energies of each conduction channel.

Judging from figure 16, the conduction channel with low activation energy 0.1–0.2 eV dominates at low temperatures, while the channel with high activation energy 0.5–0.8 eV

dominates at high temperatures. The former and the latter were designated by Philips researchers as grain conduction and pore conduction, respectively. At low temperatures newly produced electrons in the cathode move towards vacuum either along the grain surface or through the oxide grain. At high temperatures they move through pores between grains, being accelerated by the electric field and producing and multiplying secondary electrons on the way. These electrons with different origins can be identified by electron energy analysis [70]. The electrons carried by the grain conduction exhibit a nearly monochromatic distribution in energy, while pore conduction electrons show a broad energy spectrum. Adding CaO to BaO also broadens the energy distribution.

4.3.4. High current density oxide cathode. A drawback of using oxide cathodes is the limitation of the current density obtainable. Due to the material's low electrical conductivity and resulting Joule heating at high current density, the maximum current density is limited to 1.25–2.5 A cm^{-2}. (The maximum cathode surface averaged current density is 0.5–1.0 A cm^{-2}.)

A number of improved cathodes have been devised so far to enhance the electrical conductivity. The first attempt was to coat the oxide with Ni powder [75]. This certainly improved the electrical conductivity but at the same time deteriorated the electron emission. To effectively reduce the Ni content and yet enhance the conductivity, fine Ni fibres were added to the oxide and this enhanced the electron emission capability ('oxide plus') [76]. The top emission performance of the oxide plus cathode after having improved dopants and activators is that the average dc load is 4.5 A cm^{-2} [77]. Samsung has recently developed a new type of oxide cathode in which the Ni base metal surface is coated with fine grains of Ni to make it easy for the activator to be supplied and reported that the space averaged current density 3 A cm^{-2} is obtained [78].

A quite novel idea is to add to the oxide a small amount of metal oxides such as Sc_2O_3 [79, 80]. Mitsubishi reported the average current density 2–3 A cm^{-2} by adding a small amount of Sc_2O_3 to the triple oxide materials in order to reduce the interface layer formation and, thus, to maintain a large number of free Ba atoms in the oxide [79].

Matsushita has tried to test a wide variety of 'dopants' (about 1% of additives) to be added in the binary oxide, which is coated on the Ni base metal with an extremely small amount of Mg activator. Dopants include rare-earth metal elements of group III, as well as oxides of group IV and V metal elements [80].

4.4. High current density cathodes

As mentioned in section 4.3, the current density obtainable from oxide cathodes is limited. One of the reasons for this drawback originates from the fact that the electrons are emitted from the same site at which free Ba atoms are released. This makes improvement very difficult.

To improve the oxide cathode capability, dispenser cathodes were developed at the Philips Research Laboratories from the 1950s to 1960s. In these cathodes the electron emission site is completely separated from free Ba production sites. Ba atoms are continuously supplied from a reservoir to the metal surface from which electrons are emitted. Although the dispenser cathode is capable of providing a high current density, 5–10 A cm^{-2}, the operation temperature is rather high, 1000–1100 °C compared with the oxide operation temperature 700–800 °C. High temperature operation deteriorates cathode components, reducing reliability and increasing the production cost as well as spoiling the operating environment of vacuum devices. There are two types of dispenser cathodes, the L cathode and the impregnated cathode which

Table 1. The history of L-type dispenser cathodes.

Dispenser cathodes
(1) L cathode [32]
(2) Metal capillary (MK) [83]
(3) Controlled porosity (CPD) [84]
(4) CPD coated with Os/Ru [84]

will be discussed separately. Recently developed scandate cathodes enable us to reduce the operation temperature without losing the high current density capability. For details, it is recommended the reference by Cronin be consulted [81].

4.4.1. L cathode and its derivatives

L cathode. The first dispenser cathode invented at Philips is called the L cathode after the first character of the inventor's last name [82]. The cathode consists of a porous sheet of W lid welded to a Ta cavity in which Ba carbonate powder ($BaCO_3$) is filled. By heating the cathode externally, utilizing a heater, Ba atoms decomposed from $BaCO_3$ in the cavity evaporate, leak through holes in the lid and build a low work function (about 2.1 eV) monolayer on the W surface. As there is no Joule heating limit, a dc current density as high as 10 A cm^{-2} becomes possible.

Many drawbacks, however, were found later in the L cathode structure. Firstly, the Ba vapour leaks into vacuum through defects in the welded lid. Secondly, there is only a small temperature tolerance in out-gassing and $BaCO_3$ decomposition. Thirdly, poor heat conductance requires a large heating power necessary to heat the electron emitting surface.

MK cathode. Later, Siemens invented a new type L cathode to improve the original L cathode [83]. In the new cathode referred to as the MK cathode after Metall Kapilar (in German), BaO reduced in advance from $BaCO_3$ is filled in the cavity together with W capillary which serves as a reducing agent for BaO as well as a pass way for Ba atoms migrating to the lid surface. Electron emission is further improved by coating the W lid surface with an Os thin film [83].

Controlled porosity dispenser cathode. To further improve the MK cathode, BaO in the MK cathode is replaced by a triple mixture of BaO, SrO and Al_2O_3, and the porous W lid is replaced by a W thin film 20–30 μm in thickness in which regularly arranged holes several micrometres in diameter are drilled by a laser beam [84]. Electron emission of this cathode, referred to as the controlled porosity dispenser (CPD) cathode, with a work function of about 2.0 eV is further improved by coating the surface with a thin film of Os/Ru alloy [84]. The work function of the alloy coated version is about 1.8 eV.

All the dispenser cathodes discussed above are tabulated in table 1.

4.4.2. Impregnated cathodes and their derivatives

Standard (A, B and S Types) impregnated cathodes. Impregnated cathodes were invented at Philips Research Laboratories to supplement the L cathode. Instead of using a cavity reservoir

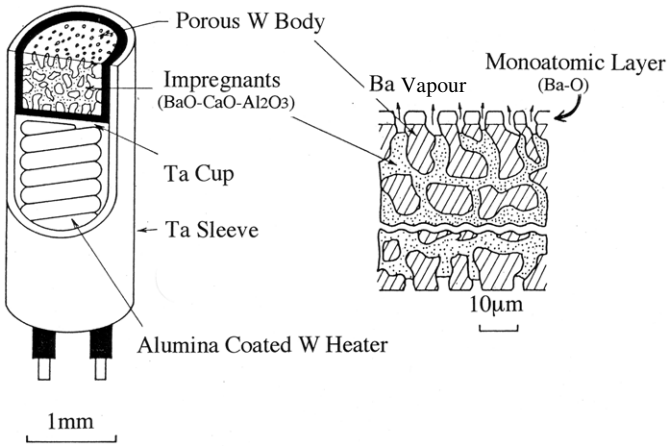

Figure 17. Schematic view of standard impregnated cathode.

as in the case of the L cathode, electron emissive materials are impregnated under hydrogen atmosphere into a porous W body as shown in figure 17 [85].

The electron emissive material, commonly named the 'impregnant', is either a binary mixture of $BaCO_3$ and Al_2O_3, A type, or a triple mixture of $BaCO_3$, $CaCO_3$ and Al_2O_3, B type or S type depending on the molar ratio of 5 : 3 : 2 (B type) or 4 : 1 : 1 (S type). During operation the reduced impregnant reacts with W in the pore to release free Ba through the following reaction in the case of the B type impregnated cathode.

$$5BaO_3 3CaO 2Al_2O_3 + W \rightarrow 2BaAl_2O_4 + \tfrac{3}{4}Ca_2BaWO_6 + \tfrac{1}{4}Ca_3WO_6 + \tfrac{9}{4}Ba + \tfrac{3}{4}Ca. \quad (36)$$

Free Ba atoms diffuse through pores to reach the cathode surface, where after combining with oxygen atoms a monolayer of BaO is formed with a low work function, about 2.1 eV.

In order to maintain the BaO surface coverage, it is necessary that Ba atoms after having been released in the pore and supplied to the surface do not evaporate from the surface before diffusing to a neighbouring pore site. The average diffusion distance of the Ba atom travelling during the lifetime τ is given as below according to the diffusion theory.

$$\sqrt{4D\tau}, \quad (37)$$

where D is the diffusion coefficient and τ the mean residence time of the Ba atom on the surface as given by (33).

Therefore, a necessary condition for maintaining the Ba coverage becomes

$$\sqrt{4D\tau} \geqslant r_0, \quad (38)$$

where r_0 is the average distance between neighbouring pores, which can be optimized by controlling the porosity of the substrate porous W sponge. As both D and τ depend on the operation temperature, the porosity of the W sponge as well as the operation temperature have to be determined to maintain the optimum Ba coverage on the surface.

M cathode. Ten years after the invention of impregnated cathodes, Philips again announced the discovery of a new impregnated cathode, which is a standard impregnated cathode coated with an Os thin film 0.1–1.0 μm in thickness. It was found that the new cathode provides an extraordinarily high current density so that with this cathode the operation temperature can

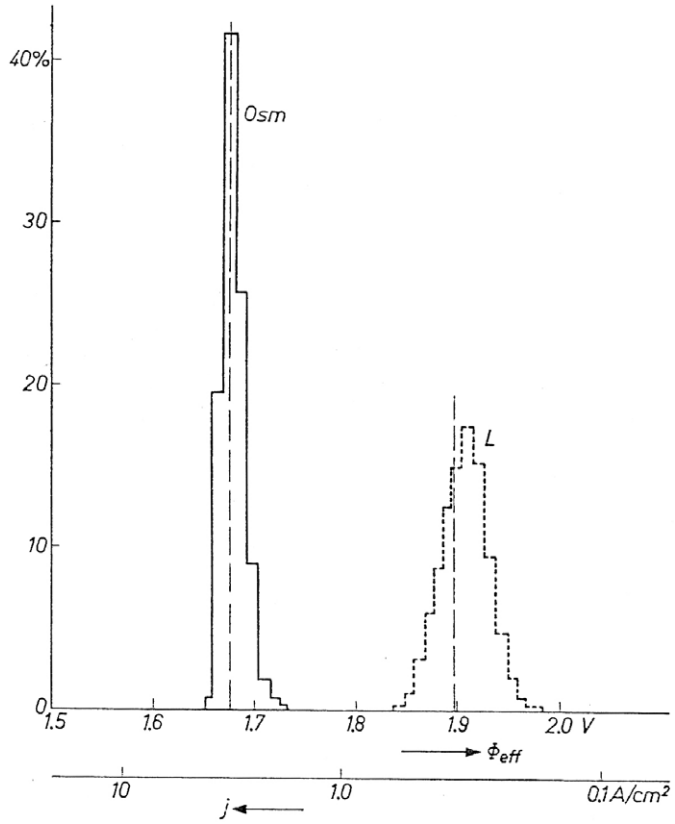

Figure 18. Comparison between L cathode and M cathode of the microscopic work function distribution (after [86]).

be reduced as much as 100 °C to sustain the same current density [86]. The improvement was so revolutionary that the cathode has since then been named a 'Magic cathode', or an 'M cathode'. Since its discovery the M cathode has been extensively used till today in a wide range of applications.

The main reasons for the emission improvement in the M cathode are depicted in figure 18, where the histogram of local work functions (not on the atomic scale at this time) on the cathode surface is plotted for the M cathode and compared with the L cathode [86]. Major points of difference seen in the figure are (1) the average work function is 0.2–0.3 eV lower for the M cathode than the L cathode and (2) the dispersion of the work function is much less in the M cathode. The coated film reduces the work function as well as making the work function uniform on the surface. As OsO_4 is toxic, an alloy of Os and Ru, Os/Ru, is more often used instead of Os alone. Other coating materials such as Ir, Re and Ru are also found effective in enhancing the electron emission. An impregnated cathode coated with Ir is manufactured and commercialized by Toshiba [87]. An exception is the Pt coating, with which the emission current is degraded. The reason will be discussed later.

CD cathode. After a certain time of operation of the M cathode, electron emission was found to be enhanced, which is considered to be attributed to alloying of the noble metal coating with the W substrate. Based on this knowledge, a new cathode referred to as the controlled

Table 2. The history of impregnated dispenser cathodes.

Impregnated dispenser cathodes
(1) Original impregnated cathode [33]
(2) Os/Ru coated cathode [34] (M cathode)
(3) 55%0s/45% W coated cathode [88] (controlled doping (CD) cathode)
(4) Mixed matrix (W/Os) cathode [90] (MM cathode)
(5) MM cathode coated with Os film [91] (coated mixed matrix (CMM) cathode)
(6) Mixed matrix scandate cathode [97]
(7) Top layer scandate cathode [98, 99]
(8) LAD top layer scandate cathode [102]

doping (CD) or the CD cathode was devised by coating the standard impregnated cathode with the alloy 55%Os/45%W [88, 89].

Mixed matrix cathode. As the M cathode is not robust enough against ion bombardment often encountered during heavy duty use, the mixed matrix cathode or the MM cathode was devised. The cathode is composed of a mixed matrix body of W and a noble metal element in which electron emissive materials are impregnated [90]. During operation, the surface is gradually coated with the noble metal by segregation of noble metal atoms from the alloy. The coating is continuously replenished even under heavy ion bombardment.

Coated mixed matrix cathode. As it takes a long time by segregation to form a noble metal coating on the MM cathode, the cathode is modified in such a way that the surface is covered with Os [91] or W [92] in advance. These cathodes are called coated mixed matrix cathodes or CMM cathodes.

All impregnated dispenser cathodes discussed above and the following scandate cathodes are tabulated in table 2.

4.4.3. Scandate cathode. Obtaining an impregnated cathode with a work function as low as that of the oxide cathode is the ultimate goal of the high current density cathode research. The scandate cathode is one of the most promising impregnated cathodes that shows the lowest work function ever achieved in the history of impregnated cathodes.

It had been well known since the late 1950s that adding Sc_2O_3 to emissive materials, especially to the impregnants, would improve electron emission [93–95]. It was in the late 1970s that the Philips group made the first attempt to evaluate the electron emission capability of a sintered barium scandate ($Ba_3Sc_4O_9$) cathode [96]. Later in the late 1980s a high emission current density was reported by utilizing the MM cathode with a small amount of Sc_2O_3 in the matrix [97]. Then, impregnated cathodes were investigated with the top layer consisting of a mixed matrix [98], a (W + Sc_2O_3) thin film [99, 100], a (W + $Sc_2W_3O_{12}$) thin film [101] prepared by sputtering and a top layer of Re/Sc_2O_3 [102]. These top layered cathodes were found to show extremely good emission and outperformed M cathodes.

Typically the top layer scandate cathodes reached 100 A cm^{-2} compared with 15 A cm^{-2} for M cathodes at the same temperature. This was even surpassed by the LAD scandate

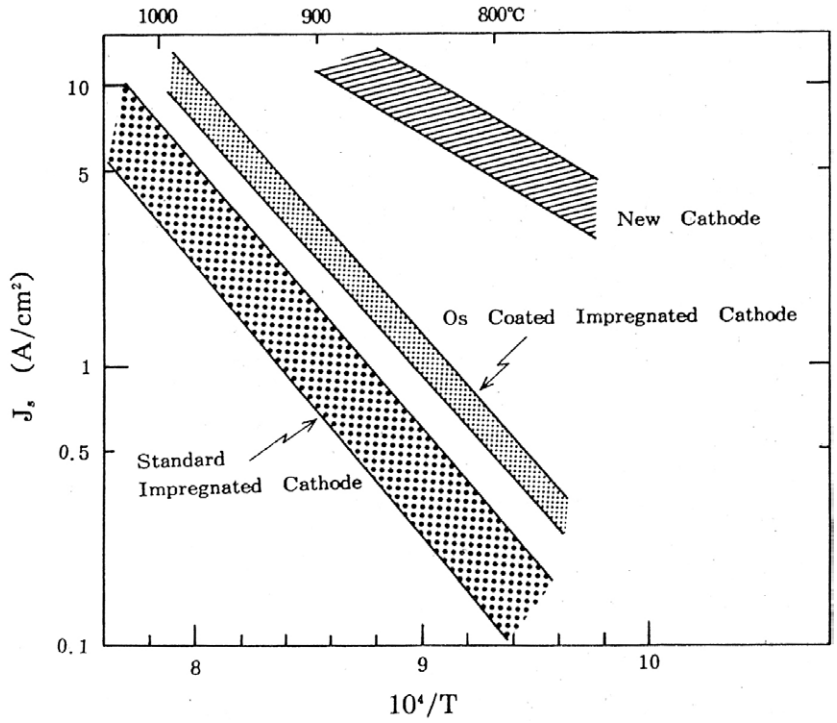

Figure 19. Saturation electron emission current density of the (W–Sc_2O_3) top layered scandate cathode in comparison with S-type and M cathodes (after [100]).

cathode of Gaertner *et al* demonstrating 400 A cm^{-2} of pulsed saturated emission under the same conditions [102]. Recently, Wang's group in Beijing (BJUT and BVERI) has developed 'sub-micron scandia doped matrix impregnated' cathodes, which provide an emission current density as high as the LAD scandate cathode [103].

Structure and electron emission. The fundamental structure of the (W + Sc_2O_3) top layered impregnated cathode is a standard S-type impregnated cathode coated with a top layer 50–400 nm thick of a W film containing 2–4 wt% Sc_2O_3 [100]. During operation a monolayer of the Ba–Sc–O complex is formed on the surface, in which Ba atoms are supplied from the substrate through the reaction given by (36), while Sc atoms are supplied through the reaction with Ba atoms and the top layer material as will be described later. O atoms are supplied from elsewhere. Figure 19 shows the Richardson plot where the emission capability of the scandate cathode is compared with those of the S-type cathode and the M cathode fabricated from the S-type standard cathode [100]. The superior emission capability of the scandate cathode over other cathodes can easily be recognized from the figure. For example, a current density of 10 A cm^{-2} can be obtained from the scandate cathode at about 100 °C below the M cathode operation temperature.

Work function. The superiority of the scandate cathode over other cathodes stems from its low work function, about 1 eV, as judged from the slope of figure 19. The work function calculated based on the thermionic emission data of the LAD Re/Sc_2O_3 top layer cathode is

1.16 eV [102], which agrees very well with 1.15 eV of the ($W+Sc_2W_3O_{12}$) top layered cathode directly measured by the retarding potential absolute method utilizing a field emission electron source [104].

Despite the nearly identical work function the emission current density of the scandate cathode in two groups [101] and [102] differs by a factor of five. This is considered to come from the uniformity of the work function distribution on the cathode surface. A non-uniform distribution of the work function creates a patch field between grains with different work functions, which suppresses the electron emission from the surface.

Sc supply rate. One of the drawbacks of the scandate cathode is the slow recovery of the emission current after ion bombardment that often occurs in CRTs. As mentioned before, to sustain stable electron emission the surface monolayer has to be maintained even under ion bombardment. The Ba concentration is maintained even under ion bombardment because the Ba supply rate overwhelms the loss by ion bombardment at the operation temperature. It is experimentally proved to be true in the case of the scandate cathode [105].

The main difficulty is the small supply rate of Sc atoms. It is found that in the case of the ($W + Sc_2O_3$) top layered scandate cathode oxidation was found necessary in order to obtain good stable electron emission [106]. The WO_3 formed by oxidizing the top layer reacts with Sc_2O_3 to produce $Sc_2W_3O_{12}$ as follows:

$$Sc_2O_3 + 3WO_3 \rightarrow Sc_2W_3O_{12}. \tag{39}$$

It was proved experimentally that $Sc_2W_3O_{12}$ thus formed releases free Sc atoms through the following reaction with Ba [101, 106]:

$$Sc_2W_3O_{12} + 3Ba \rightarrow 2Sc + 3BaWO_4. \tag{40}$$

It is found that the above reaction is completed by heating the cathode for about 2 h at 1150 °C, and the activation energy is estimated to be about 4.6 eV [105]. A future issue in improving the Sc recovery rate will be to devise how to reduce the activation energy to release free Sc atoms in the top layer at an operating temperature as low as 850 °C.

4.4.4. Theoretical aspects of cathode operation. As the theories related to oxide cathodes are already stated in section 4.3, those on dispenser cathodes will be briefly presented here.

The following are some of the authors who have reported works related to the Ba–O monolayer structure as well as the work function reduction mechanism under the influence of monolayers. They are Baum (1980) [107], Skinner *et al* (1982) [108], Haas *et al* (1983) [109], Norman *et al* (1987) [110], Mueller (1988, 1989) [45, 111], Shih *et al* (1988) [112], and Hemstreet *et al* (1988) [113].

Impregnated cathode. The group of Norman determined for the first time the structure of BaO on the B-type impregnated cathode based on the surface extended x-ray absorption fine structure (SEXAFS) measurements [110]. According to their proposed structure, as shown in figure 20, Ba sits 2.62 Å above O and the distance between Ba and four W atoms is 3.49 Å. Shih *et al* [112] and Hemstreet *et al* [113], however, rejected Norman's model based on their similar experimental results on the S-type impregnated cathode, and both groups claim that Ba must sit on the middle of three O atoms adsorbed on a W surface. According to their model structure, the Ba–O axis is slanted 60° away from the surface normal direction.

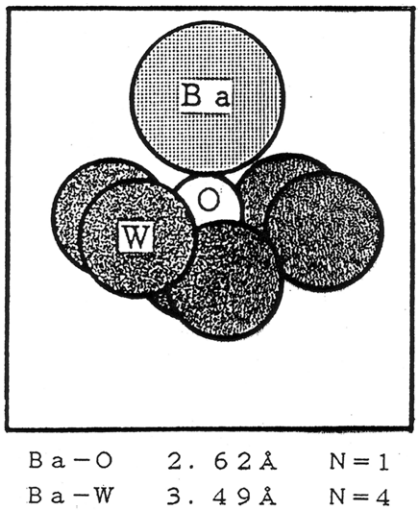

Figure 20. Norman's model of Ba–O monolayer on a B-type impregnated cathode (after [110]).

Electronic structure. Based on Norman's model structure and utilizing the relativistic Xα scattering wave method, Mueller computed the electronic structure of a cluster composed of nine W atoms in the bcc structure, one Ba atom and one O atom [45, 111]. According to his electronic structure, the Ba atom donates 1.5 electrons to the substrate W to make an ionic bond, while the oxygen atom makes a covalent bond and shares electrons with the substrate receiving only -0.2 electron charge. The O atom is found to assist the charge transfer from Ba to the substrate. The net electric dipole is formed between the Ba ion and the substrate instead of between Ba and O ions.

In order to include the interaction between dipoles at high surface coverage of Ba–O, a computation was made by expanding the cluster size to include 19 W atoms as shown in figure 21(*a*) [114]. A computed coverage dependence of the work function is shown in (*b*), in which the work function minimum of the standard cathode, Ba–O on W, is assumed to be 2.0 eV. In the figure not only Ba–O on W, but also Ba–O on Pt–W, Ir–W and Os–W are included. The cases Ba–O on Ir (hcp structure) and Os (hcp structure) mimic the M cathode.

Mechanism of work function reduction. The work function of the substrate W is reduced by the dipole field created by the Ba–O monolayer as already discussed in section 3. By coating the substrate with a thin film of noble metal elements, the bond length between Ba and the substrate is stretched. This increases the strength of the initial dipole moment as well as the bond energy. The bond stretching is confirmed by EXAFS [110]. Due to the increase in the bond energy the maximum adsorbate concentration also increases, leading to a further reduction of the minimum work function.

The only exception is the case of the Pt coating, where due to the closely packed nature of the Pt fcc structure the depolarization of dipoles is enhanced leading to the reduction of the bond energy and the adsorbate concentration. This results in an increase in the minimum work function.

Scandate cathode. There are not many theoretical and experimental works reported on the geometrical as well as electronic structure of the scandate cathode. Two structure

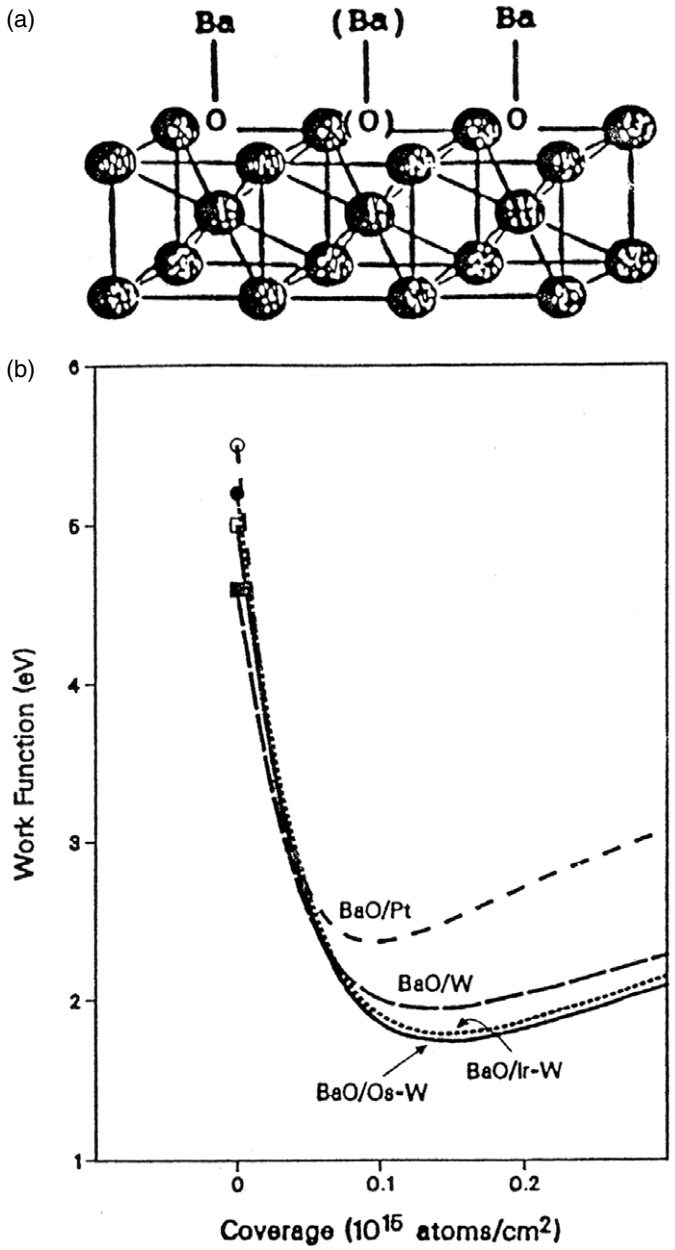

Figure 21. Cluster model of impregnated cathode coated with various metal elements (*a*) and the Ba–O coverage dependence of the work function (*b*) (after [114]).

models are proposed: (1) the Ba–Sc–O monolayer model [45, 105] and (2) the adsorption model Ba–O/Sc_2O_3 [115]. Following is the theoretical computation by Mueller based on the relativistic Xα scattering wave method [116]. Figure 22 shows the model used in the computation (*a*) and the Ba coverage dependence on the work function (*b*).

In his model computation a cluster of 25 W atoms (16 in the first layer, 9 in the second layer), four Sc atoms and five O atoms, both in the first layer, is used. The number of Ba atoms

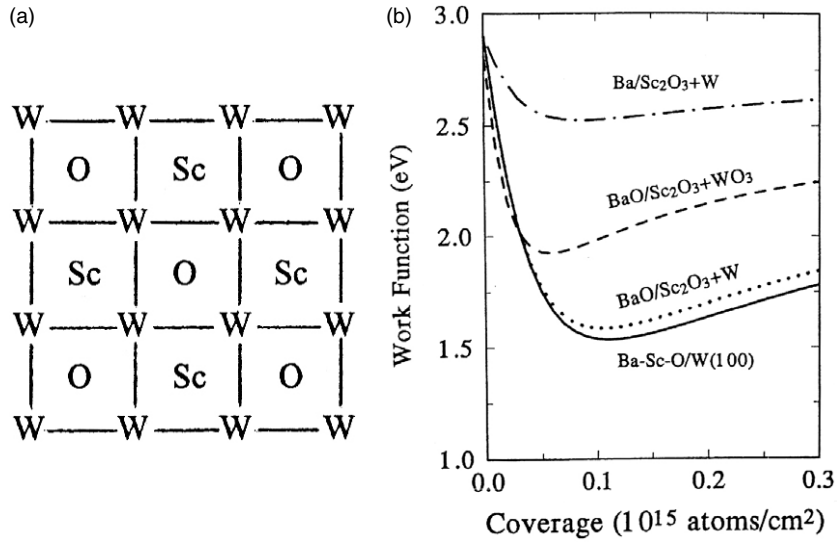

Figure 22. Cluster model of the scandate cathode (*a*) and Ba coverage dependence of the work function (*b*) (after [116]).

varies from 1 to 5 corresponding to the coverage. The result does not show any distinctive difference in either model. The computed minimum work function is much larger than that measured [102,104]. Furthermore the minimum work function is attained at a very low surface coverage, which does not agree with the experimental result [96].

A peculiar feature of the scandate cathode is the monolayer Ba–Sc–O which can be attained only when free Sc atoms are released. According to the experiment in which the electron emission as well as the surface atom composition of the MM cathodes with a W body containing various rare-earth oxides was measured, only the MM cathode containing Sc_2O_3 showed an excellent emission capability [117]. Only on the surface of the MM cathode with Sc_2O_3, was the Sc monolayer detected. Although Mueller claims that good emission must be obtained by replacing Sc with Y [116], the most important prerequisite the author believes is if free Y atoms are released to form a monolayer.

Apart from the two models discussed above, Raju and Maloney proposed a semiconductor model [118] in 1994, which has recently been reconsidered by Shih [119], Wang [120] and Gaertner [121] based on their experimental results.

5. Historical review of field emission materials

Although field emission electron sources have such advantages over thermionic emission electron sources as high brightness, high monochromaticity and low power consumption, several critical conditions are requested for the material. The material has to withstand high temperature due to Joule heating that limits the maximum current density obtainable from a field emitter. The material must also withstand high tensile stress $f = F^2/8\pi$ exerted on the material by the applied electric field F to draw a field emission current. The material is required to hold a high enough surface tension or a surface energy to sustain the shape of the tip apex under high electric field. This is a very important issue especially when a field emitter is operated at high temperatures. The fourth and the most important requirement is the high

emission current stability. Refractory metals satisfy all the above requirements except current stability.

Two major current instabilities reported are the flicker noise type and the step and spike type current fluctuations. The major origin of the current fluctuation in field emission is that unlike thermionic emission, the elemental processes such as randomness and statistical fluctuation of electron emission are not protected by the space charge. Among all current fluctuations or noises, the flicker noise type fluctuation dominates the instability of the field emission from metals. In the case of carbon related materials, as will be described later, the major current fluctuation is the step and spike type that is caused by ion bombardment of the surface by ambient gas ions created by the field emission current.

5.1. History of field emission materials

The first observation of field emission from metals was made by Lilienfeld in 1922. The theoretical foundation of field emission was given by Fowler and Nordheim in 1928. In 1937 Mueller discovered the field emission microscope, which has since enabled one to observe microscopic structures of the field emission tip apex.

In the late 1960s Crewe and his group first applied a W field emitter to the electron source of high resolution electron microscopes [122]. In order to reduce current drift and fluctuation, specific to field emission from metals, operation under ultra-high vacuum was necessary. Later on, in the search for field emission materials with less current fluctuation, carbon related materials were investigated but were not used extensively because of the other type of current fluctuation, the step and spike type current fluctuation. As this fluctuation is found to increase with the product of emission current and operation pressure, again they are limited to be low. Carbon related materials, however, have been attracting researchers' attention since the discovery of diamond-like carbon (DLC) and CNTs and their application to the field emission display (FED).

Various monolayer type field emission materials were invented that are capable of working under relatively poor vacuum conditions while a high current density can be drawn. The Zr–O monolayer field emitter [35] pioneered by Swanson has been used quite extensively since its invention in the field of electron beam machines and surface analysis instruments. The Ti–O monolayer field emitter [123] was also found to work as well. Recently, the Y–O monolayer field emitter has been proposed [124].

The low work function Zr–O monolayer adsorbed on the (100) plane of a W single crystal substrate is continuously replenished even under heavy ion bombardment. To supply a stable monolayer on the substrate, the material is operated at high temperatures, which causes the monochromaticity of the electron beam to deteriorate. To reduce the operation temperature, a Mo substrate is proposed to replace the W substrate [125]. The monolayer field emitters, however, may not be good candidates for electron sources of vacuum nano-electronics because of their high temperature operation, complex operation mechanism and difficult mass production.

To reduce the current fluctuation, a field emitter array (FEA) was invented by Spindt in the middle of the 1960s [126, 127]. Current fluctuation is statistically reduced by ensemble averaging the current from many identical field emitters. Many identical Mo field emitters are deposited on a substrate utilizing a specially designed deposition technique. In the 1980s, 15 years after the first FEA, a high packing density Si-FEA was fabricated on a Si substrate by utilizing a modern Si device fabrication technology [128]. The reduction of the current fluctuation by ensemble average was experimentally proved by the Si-FEA [129].

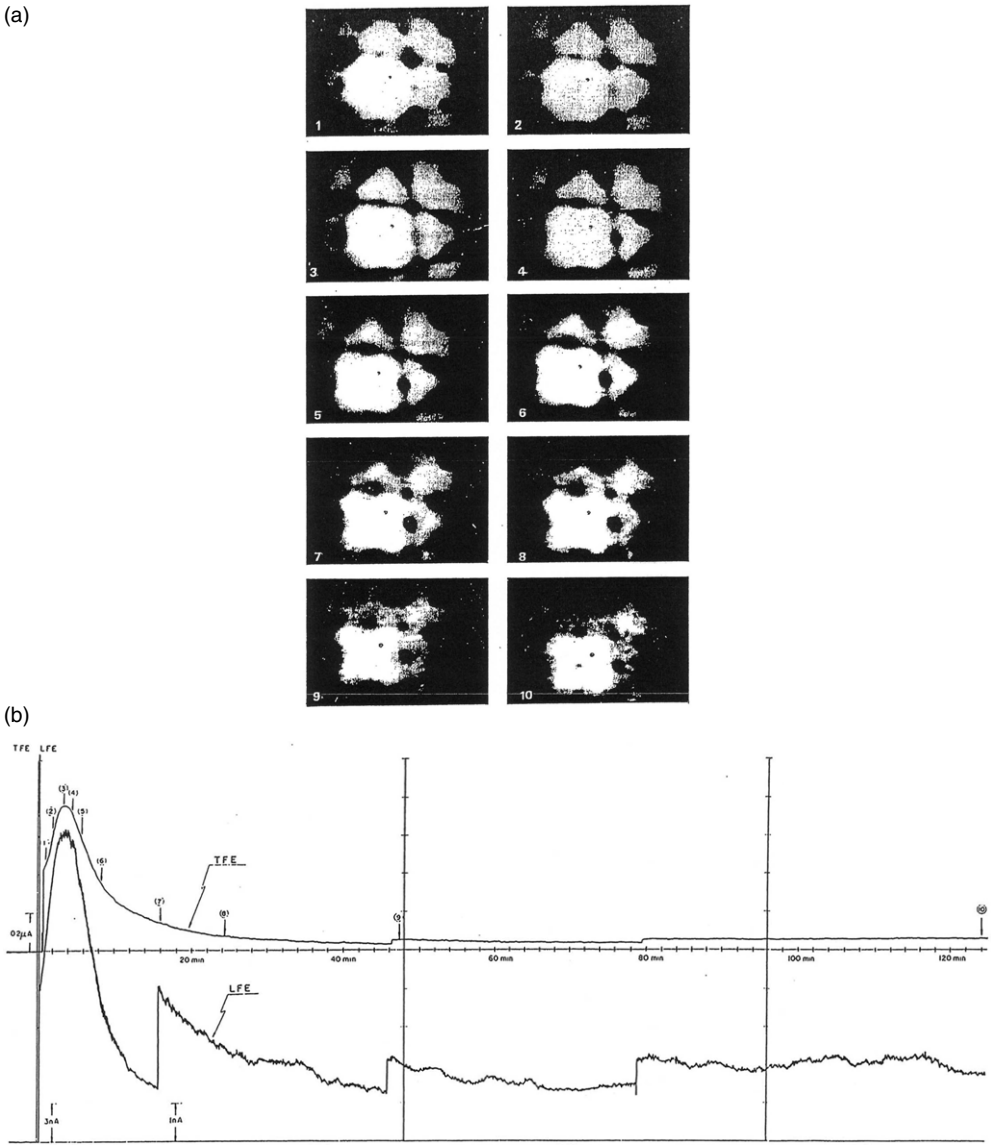

Figure 23. Change in time of the FEM image obtained from a W field emitter oriented to the (310) direction (*a*) and the corresponding change in time of total (TFE) and local (LFE) field emission currents (*b*) (after [131]).

The current fluctuation is considered to be induced by the change in time of the local work function and/or the field strength on the atomic scale that is caused by adsorption, desorption, surface migration and ion bombardment of ambient molecules.

5.2. Field emission current fluctuation from metal field emitters

5.2.1. Flicker noise type current fluctuation. A series of spatial distributions of field emission, called the field emission micrograph (FEM), from a W tip and the corresponding current

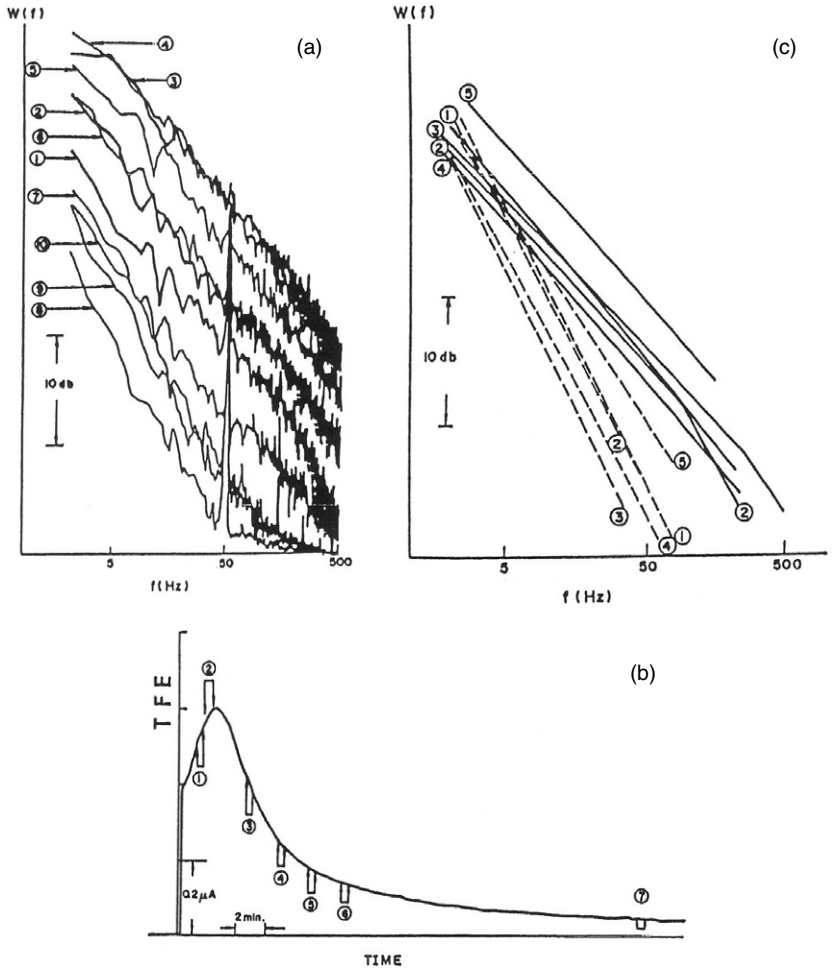

Figure 24. PSD of the current fluctuation measured at the probe hole (*a*), time and duration of PSD measurements (*b*) and results of repeated PSD measurements at the early (——) and the later (- - - -) stages (*c*) (after [131]).

drift/fluctuation are presented in figures 23(*a*) and (*b*), respectively [130]. The W field emitter is a W single crystal oriented to the ⟨310⟩ direction, which is polished into a sharp needle 100–200 nm in radius. The FEM is a micrograph with an extremely high magnification of over a million times and displays the spatial distribution of various surfaces with different work functions. Only a limited portion, a dark spot at the centre, of the electron emission from the (310) plane is utilized as an electron source for the electron microscope. Data were taken first by flash cleaning the field emitter surface and then by applying an electric field to the emitter. The FEM and the emission currents, both the total current TFE and the local current LFE from the probe hole, change with time by the adsorption of ambient gas molecules such as H_2 and CO. After having passed through the early maximum, the field emission current decreases with time and then the LFE current fluctuation starts to increase. To maintain the current level, the applied field is raised three times as can be seen in (*b*) during operation in this experiment. In order to analyse the current fluctuation, the power spectrum density (PSD) (figure 24(*a*)), is measured for the local field emission current, LFE, at various running times (*b*). The PSD

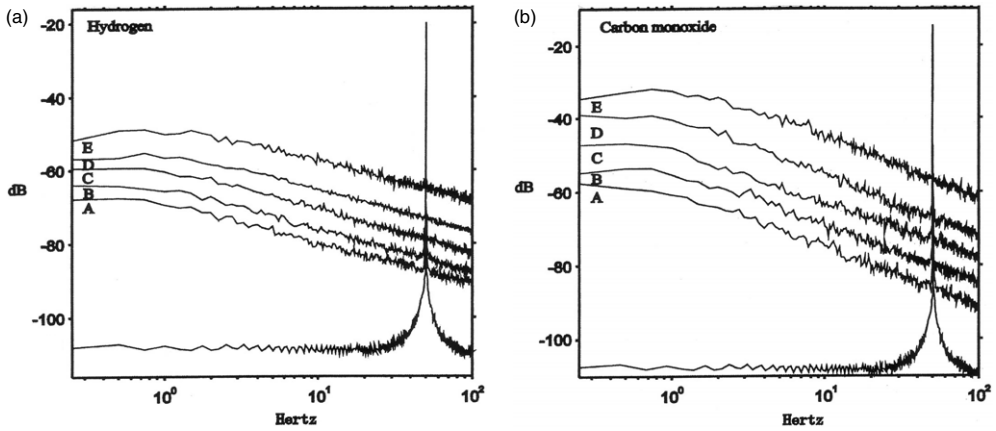

Figure 25. Ambient pressure dependence of the PSD obtained from the field emitted current fluctuation of the Si-FEA: (*a*) for H_2 and (*b*) for CO ambient (after [130]). (Partial pressures are $A = 10^{-9}$ Torr, $B = 10^{-8}$ Torr, $C = 10^{-7}$ Torr, $D = 10^{-6}$ Torr and $E = 10^{-5}$ Torr.)

presented here is the time average in the data acquisition time of 30 s. From the obtained PSDs, one can find that the current fluctuation is the flicker noise type, that the PSD reaches the maximum at the inflection point of the time varying current and that the slope of the PSD changes from -1 at the early stage of operation to -1.5 at the later stage. The experiment was carried out many times to make sure the change in slope is real as shown in figure 24(*c*), in which solid and dotted lines are the data taken at the early and the later stages, respectively. It was also found, not shown in the figure, that the slope depends on the type of gas introduced in the test chamber: -1 for H_2 and -1.5 for CO [131].

The change in the slope can be understood as follows. H_2 adsorbs on the emitter surface at first because H_2 is the major ambient gas component, then it is replaced later by CO, the second major ambient gas component that has a greater adsorption energy than H_2. The maximum seen in the PSD can be explained in terms of the transition rate of migrating atoms and molecules on the surface as will be discussed in detail later.

Interestingly enough, a similar current fluctuation can be found in the Si-FEA as shown in figure 25, in which the PSD of the current fluctuation is measured in H_2 (*a*) and CO (*b*) of various ambient pressures [129]. Here one can again find the difference in the slope of the PSD: -1 for H_2 and -1.5 for CO regardless of the pressure.

5.2.2. Theoretical aspect of flicker noise type current fluctuation. The change in the work function on the atomic scale that induces the fluctuation in the field emission current is considered to arise from (1) adsorption and desorption of gas molecules, (2) a change in the number density of adsorbed molecules in a patch from which electrons are field emitted and (3) migration of adsorbed molecules in and out of the patch on the surface. Among them, (2) and (3) are the most probable and here case (3) will be discussed as follows.

It is well known from temperature programmed desorption (TPD) experiments that there are a number of adsorption sites, each having different desorption energies, and it is reported that these multiple adsorption sites influence the current fluctuation [132]. When an adsorbed molecule moves from one site to another site having different desorption energy, and hence different work function on the atomic scale, then the work function must change with time, introducing a macroscopic change in the field emission current.

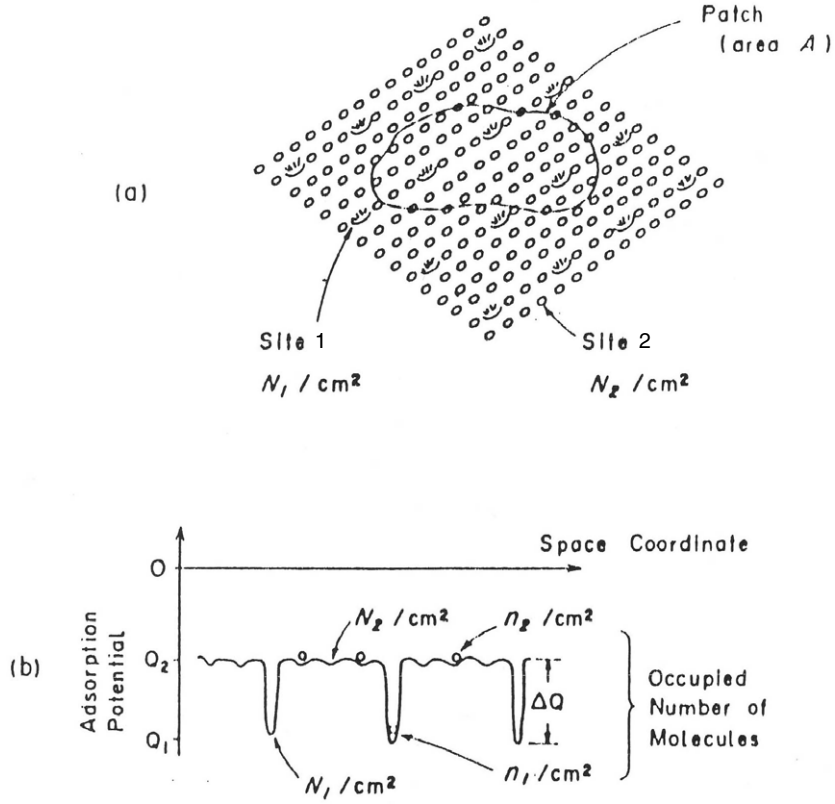

Figure 26. Two-site model for the field emission current fluctuation. (Area of electron emission (patch) (*a*) and two independent sites with different desorption energies in the patch (*b*) are indicated.)

The first step to obtain the PSD of the current fluctuation is to find an autocorrelation function of the change in the emission current $\Delta I(t)$. For example, consider a site from which a molecule moved out and induced a change in the emission current $\Delta I(t)$ at $t = t$. If later at time $t = t + \tau$ the site is still not filled with other molecules or the molecule that left the site at $t = t$, then one obtains $\Delta I(t+\tau)$. From the product of $\Delta I(t)$ and $\Delta I(t+\tau)$ the autocorrelation function will be calculated by integrating over time. Then, utilizing the Wiener–Khinchin theorem, the PSD can be calculated by Fourier transforming the autocorrelation function thus obtained.

This is a standard classical way of obtaining PSDs. Utilizing the digital information processing technology and a fast computer, however, the PSD can be obtained directly by the fast Fourier transform (FFT) method. All experimental data shown here were obtained by utilizing the FFT method.

Kleint computed the PSD [133] for the case in which as shown in figure 26 there are two adsorption sites 1 and 2 with a difference in desorption energies ΔQ, and the adsorbed molecules do not interact with each other. In this model the number density of molecules in the patch is assumed to be unchanged. The other model, the patch model, takes into account the change in the number density of molecules in the patch [134, 135]. The calculated PSDs are reviewed in figure 27.

Power Spectrum Density (PSD)

of Field Emission Current Fluctuation

(Two-Site Model)

(1) Low Frequency Region

$$W(f) = (\Delta I)^2 K \qquad f \ll \frac{1}{T}$$

(2) Intermediate Frequency Region

$$W(f) = (\Delta I)^2 K f^{-(2-\chi)}$$

(3) High Frequency Region

$$W(f) = (\Delta I)^2 K f^{-2} \qquad f \gg \frac{1}{t_0}$$

$\chi \cong \dfrac{\lambda}{\pi l}$

$\lambda =$ 2-Dimensional capture cross-section

$l =$ Distance between different adsorption sites

$K =$ Transition rate

$\Delta I = \dfrac{3}{2} B I \phi^{1/2} \dfrac{\Delta\phi}{F}$ (Fowler-Nordheim Term)

Figure 27. PSD calculated by Kleint based on the two-site model.

According to the results shown in figure 27, the PSD is proportional to ΔI^2 and K in all frequency regions, in which ΔI, the Fowler–Nordheim term, is given by (41) from the Fowler–Nordheim equation when the work function on the 'atomic scale' changes by $\Delta\phi$:

$$\Delta I = \frac{3}{2} B I \phi^{1/2} \frac{\Delta\phi}{F}. \tag{41}$$

The transition rate K reaches the maximum at certain surface coverage depending on the ratio of the number of adsorption sites N_1/N_2. Figure 24 shows that the PSD reaches the maximum at the inflection point of the time varying field emission current, where the maximum transition rate is expected to occur.

In the intermediate frequency region, a frequency dependence arises in the PSD. As the captured cross section λ of a molecule to the site 1 increases, the slope tends to decrease. Considering that initially adsorbed H_2 is replaced by CO at a later time, the captured cross section of H_2 must be much greater than CO. This is also proved by introducing both gases independently and by measuring PSDs as shown in figure 25 and in [130]. In the high frequency region, however, there is no frequency dependence in the PSD despite the kind of gas molecules adsorbed on the emitter surface.

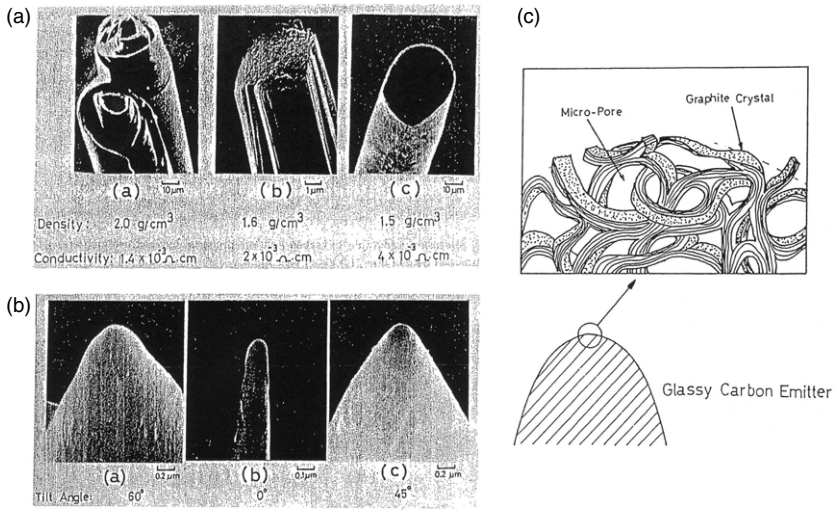

Figure 28. SEM images of whisker-like carbon fibre, commercial carbon fibre and glassy carbon fibre (*a*), TEM images of tip apex of the corresponding materials (*b*), and micro-structure of glassy carbon tip apex as sketched based on the TEM image (*c*) (after [139]).

5.3. Field emission from carbon materials

As already mentioned in the previous section, the current fluctuation is reduced by minimizing the transition rate K. This can be accomplished both by operating field emission under ultra-high vacuum or by heating the emitter to minimize the number of molecules migrating on the surface. Operation under ultra-high vacuum is sometimes inevitable because heating causes the monochromaticity of the electron beam to deteriorate.

It is well known in surface physics that carbon related materials are inert to gas adsorption and may be an ideal candidate as noise free field emitters. Some carbon materials with a high aspect ratio suited for field emission have recently been developed and applied to the FED. They are CNTs [136] and graphite nano-fibres (GNFs) [137]. Other carbon materials such as carbon whiskers, carbon fibres and glassy carbon were investigated in the past as electron sources for electron microscopes [138]. All materials show similar field emission characteristics because they are all essentially composed of graphite.

5.3.1. Step and spike type current fluctuation. Figure 28(*a*) shows the scanning electron microscope (SEM) images of carbon materials, such as a whisker-like carbon fibre, a commercial carbon fibre and a glassy carbon fibre. The transmission electron microscope (TEM) images of the above mentioned carbon fibres after chemically polished into tips are shown in (*b*). The surface structure model of the glassy carbon tip is schematically drawn from TEM images and is shown in (*c*). The tip is composed of graphite ribbons randomly distributed [138]. Figure 29 shows TEM images of (*a*) an open ended MWNT, (*b*) a GNF, (*c*) a closed ended MWNT and (*d*) a bundle of single-walled nano-tubes [136].

As seen in figure 30(*a*), the field emission current from a glassy carbon emitter is stable and flicker noise free under high vacuum, but a new type of current fluctuation (step and spike type current fluctuation) starts to appear as the operation pressure increases as shown in (*b*) [139]. The current fluctuation from a CNT emitter is shown in figure 31 under (*a*) low and (*b*) relatively high current conditions, respectively.

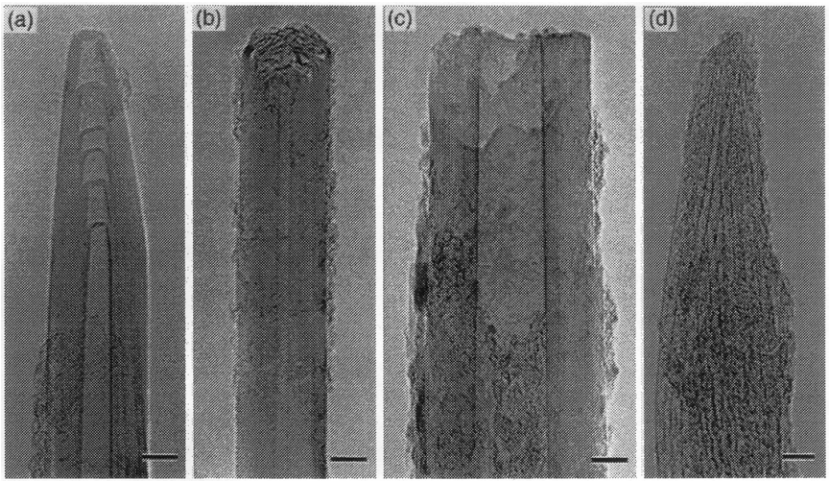

Figure 29. TEM images of CNT field emitter tips: open ended MWNT (*a*), GNF (*b*), closed ended MWNT (*c*) and bundle of single-walled nano-tubes (*d*) (after [137]).

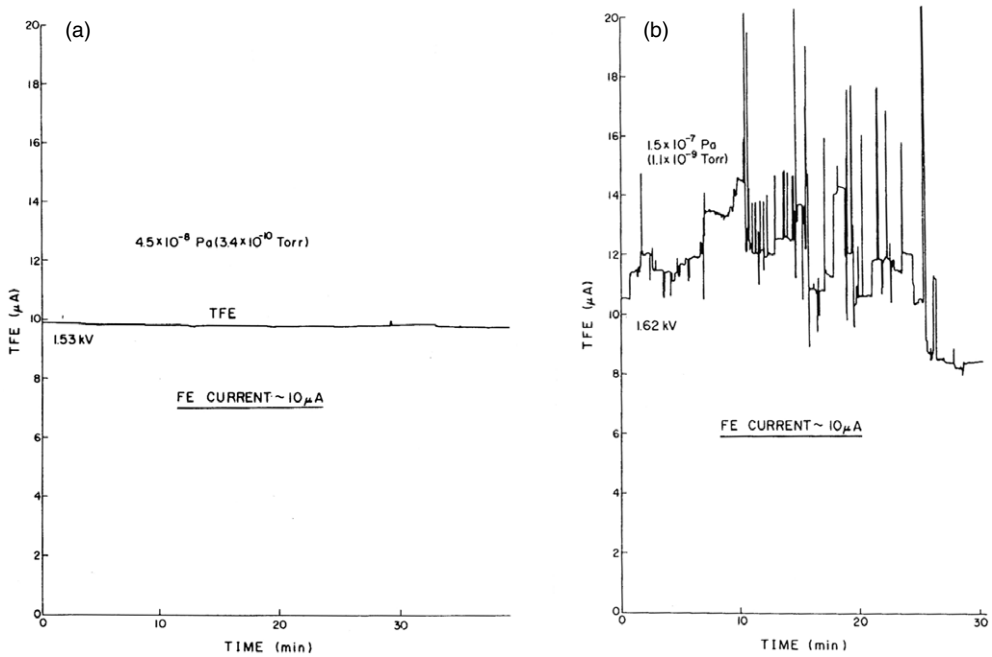

Figure 30. Field emission current from a glassy carbon field emitter operated under ultra high vacuum (*a*) and under relatively poor vacuum (*b*) (after [140]).

In both figures, the current fluctuation can be seen to increase as the operation pressure and the emission current become large. The current fluctuation, referred to as a step and spike type fluctuation, comprises steps and spikes caused by long and short time changes in the emission current, respectively. Another feature of this type of current fluctuation is the very small correlation between the total current (TFE) and the local current (LFE) obtained from

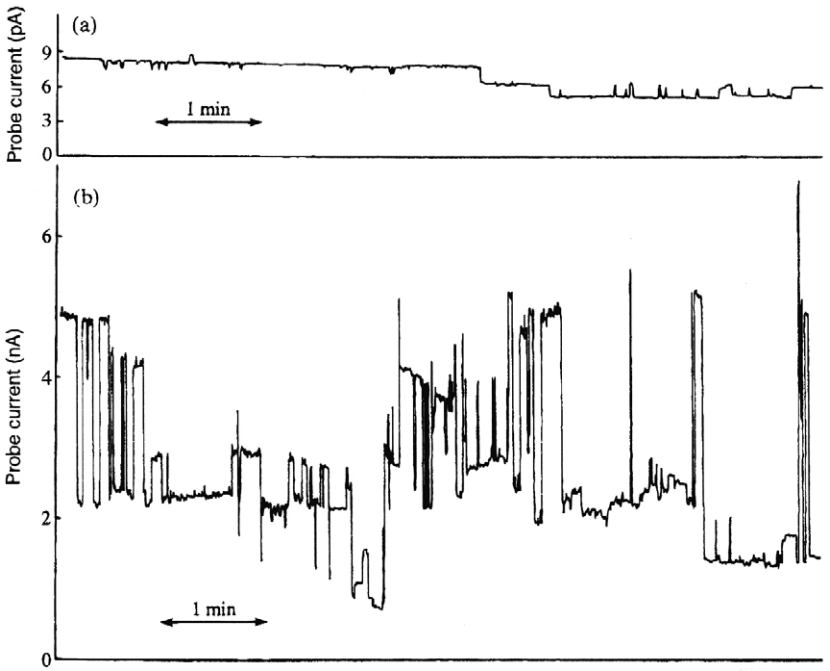

Figure 31. Field emission current from nano-tube field emitter operated under a small current condition (*a*) and under a relatively large current condition (*b*) (after [137]).

a probe hole. This is in contrast to the current fluctuation from metal emitters that is induced by a collective motion of adsorbed molecules and has a strong correlation between the changes in the TFE and the LFE. As this type of current fluctuation does not favour the PSD analysis because of the wide frequency bandwidth required for measurements, the number of steps and spikes is counted by eye for 20 min and is correlated with the product of emission current and operation pressure as shown in figure 32 [139]. A linear relationship is recognized between the number of steps and spikes and the current–pressure product, indicating that the current fluctuation is caused by the ions originating from ambient gas molecules in vacuum ionized by the field emission current. The number of steps and spikes is also found dependent on the type of gas ambient such as H_2 and CO introduced into the test chamber. CO molecules having a larger ionization cross section produce a larger number of ions by electron impact, thus creating a current fluctuation about an order of magnitude greater than H_2 molecules under the same partial pressure.

5.3.2. Mechanism of step and spike type current fluctuation. It is speculated that the source of the step and spike type current fluctuation are ions of ambient gas molecules ionized by the field emission current. Ions thus formed impinge on the emitter surface by tracing back the trajectories of field emitted electrons.

Ion trajectories. The number of ions impinging on the emitter surface that affects the current fluctuation is computed by ion trajectory analysis [140]. According to the computation, only a very small fraction of the ions coming from a small solid angle subtended by the tip impinges on the active area of the tip surface from which electrons are field emitted. The number of computed impinging ions in 20 min is shown in figure 32 as a vertical solid line extending

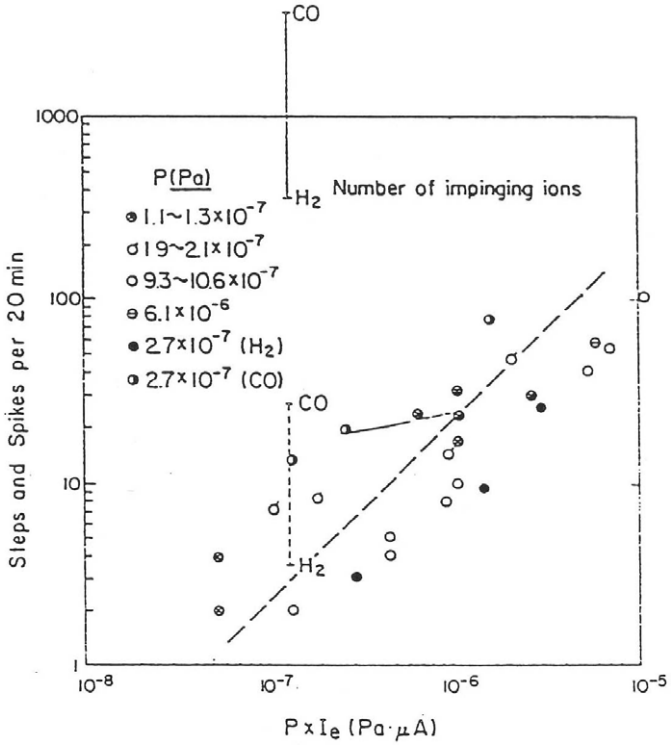

Figure 32. Step and spike current fluctuation from a glassy carbon field emitter as a function of the current–pressure product (after [140]). (The solid vertical line is the calculated number of impinging ions on the patch, while the dotted vertical line indicates the number two orders of magnitude less than the number of impinging ions.)

from CO to H_2. The actual number is, however, more than two orders of magnitude less than that calculated as shown by a dotted vertical line, meaning that not all ions trigger the current fluctuation. One of the reasons is that not all spikes can be counted because of their short duration time. If the fluctuation was caused only by ion sputtering of the electron emitting material, then only the step type current fluctuation should arise. We also know that the current fluctuation is reduced by heating the tip surface [139]. By heating the tip surface we would expect fewer adsorbed molecules on the surface than at room temperature.

Major source of current fluctuation. Based on the results mentioned above, the major cause of the current fluctuation is speculated to be the change in the work function due to adsorbed molecules either sputtered (steps) or temporally dislodged (spikes) by ion bombardment. The major adsorbed species is found to be H_2 from the recent atom-probe analysis. A recent theory based on first principles tells us that the field emission from a graphite ribbon is mainly from the surface states created by a dangling bond, and therefore the electron emission ceases when the dangling bond is terminated by H atoms [141]. It is also pointed out in the theory that H atoms terminating the dangling bond are easily removed by passing a current through the bond.

To reduce or to eliminate the current fluctuation of the step and spike type, the emission current should be reduced, the operation pressure should be reduced or the tip should be heated to remove adsorbed H_2 molecules.

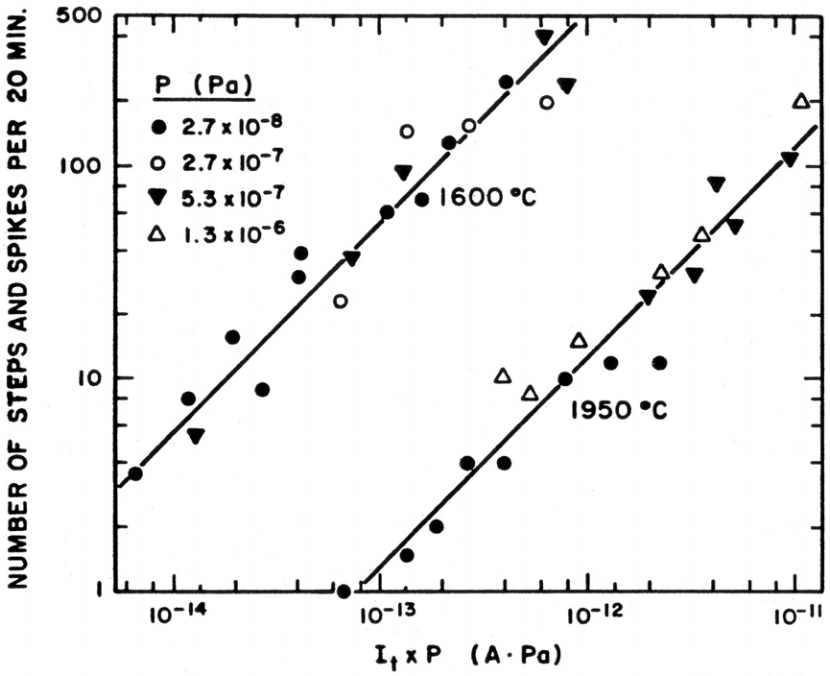

Figure 33. Step and spike current fluctuation from a TiC field emitter as a function of the current–pressure product (after [144]). (The fluctuation depends strongly on the flashing temperature prior to operation as indicated in the figure.)

Transition metal carbides. A similar argument can also be made for transition metal carbides. When the topmost layer of the carbide surface is composed of all carbon atoms the current fluctuation is the step and spike type, while the flicker noise type fluctuation is dominant when the top layer is composed of metal atoms [142]. After having counted the number of steps and spikes of the current fluctuation obtained from a TiC(100) field emitter, Adachi *et al* [143] plotted them with the current–pressure product and found a linear relationship as shown in figure 33 just as in the case of glassy carbon field emitters. They report that the current fluctuation depends on the crystalline perfection, the impurity content, the stoichiometry and the way the high temperature flashes. Ishizawa *et al* conclude that the current stability depends mostly on the surface treatment and that the surface with a monolayer of graphite on top presents the best current stability [144].

Diamond field emitters. In this report, diamond field emitters are excluded from discussions, although diamond is one of the promising candidates for an ideal field emitter. One of the reasons is that there are not enough reliable experimental data and theoretical analyses in this field. Most of the electron emission data are from the 'diamond like carbons' of chemical vapour deposition (CVD) diamond films that are not well characterized, as far as the author understands. The emission current fluctuation from diamond field emitters has not been reported. Besides, the electron emission mechanism remains uncertain. There are, however, a few theoretical works recently published based on first principles that should not be neglected. Watanabe *et al* claim [145] that the the electron emission from diamond is enhanced by the H termination of dangling bonds, in contrast to the case of CNTs and other carbon related

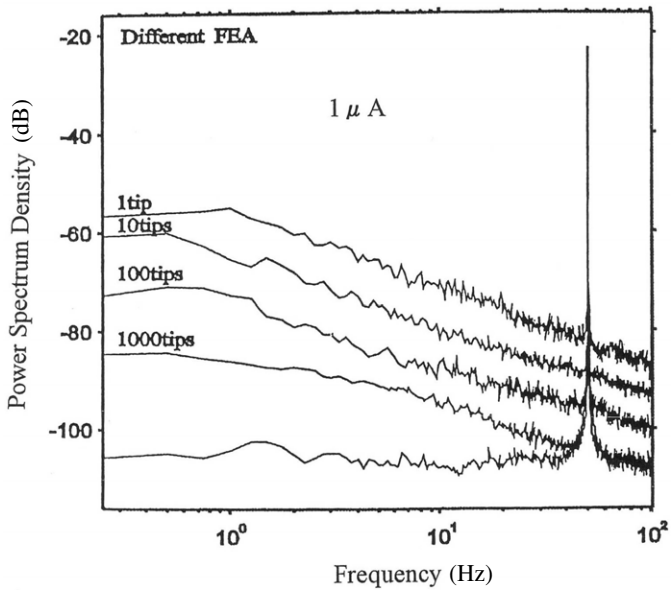

Figure 34. PSDs of the current fluctuation from the Si–FEA with different tip numbers operated under the same emission current 1 μA (after [130]).

materials, where H termination suppresses the electron emission. According to their theory, unlike CNTs, occupied bulk states contribute to the electron emission rather than the surface states created by dangling bonds. This result qualitatively agrees with the experimental results obtained from CVD diamond surfaces with graphitic patches [146]. A major disadvantage of diamond field emitters for practical applications is that the emission current is limited due to the low electrical conductivity of diamond.

5.4. Reduction of current fluctuation by ensemble averaging

Spindt *et al* of SRI invented a novel field emitter called the FEA that is composed of many identical emitters [126, 127]. By ensemble averaging, the PSD of the current fluctuation must be reduced by a factor corresponding to the number of emitters that operate simultaneously. The reduction of the PSD by ensemble averaging is experimentally verified utilizing the Si-FEA as shown in figure 34 [129]. The PSD of the flicker noise type current fluctuation is seen to be suppressed by 10 dB by every multiple of the tip number of 10 under the identical emission current condition. The result also proves that the flicker noise type current fluctuation is purely statistical. Concerning the step and spike current fluctuation, it is not certain if the ensemble averaging is effective or not.

6. Summary

In most of the present day industries, thermionic emission materials are exclusively used in such fields requiring high current density and high reliability as CRTs, transmission and receiving tubes, x-ray sources and various electron beam machines. Field emission electron sources on the other hand, since applied to a high resolution electron microscope in the 1970s, have been applied and replaced thermionic emission sources in a wide variety of fields of electron

beam machines that require high brightness and high spatial resolution. Following the trend towards high brightness electron sources, field emission will attract more and more attention in the future. For space applications, vacuum tubes with either thermionic or field emission cathodes are far superior to solid state devices due to their longer life and higher resistance against radiation damage.

The point that the author wants to stress in this report is the deep involvement of surface physics in the field of electron emission. It is well known that surface physics has been in touch with electron emission since its birth in the 1960s. Nowadays, analysing the surface on the atomic scale is indispensable for the understanding and development of electron emissive materials. Moreover, assisted by various modern measurement techniques, and theories based on first principles, the qualitative understanding of electron emission in the past is now becoming more and more quantitative.

Acknowledgments

This report would not have been possible without the moral as well as financial support of the National Institute of Advanced Industrial Science and Technology (AIST). The author is deeply indebted to Dr Junji Itoh, the Deputy Director of Planning Headquarters, and Dr Kunihiko Yamaji of Nano-Electronics Research Institute, both in Tsukuba research centre. The author thanks Professor Masahiro Sasaki of the University of Tsukuba for various suggestions and comments and Mr Takanobu Sato, a graduate student at the University of Tsukuba, for technical assistance during the course of compiling figures used in this report.

Finally, the author would like to thank all the referees of this paper for their productive suggestions and comments which have helped the author in improving the manuscript.

References

[1] Richardson O W 1912 *Phil. Mag.* **23** 594
[2] Wehnelt A 1904 *Ann. Phys., Lpz.* **14** 425
[3] Wilson A H 1931 *Proc. R. Soc. Lond.* **133** 458
[4] Nottingham W B 1956 *Handb. Phys.* **21** 1
[5] Murphy E L and Good R H Jr 1956 *Phys. Rev.* **102** 1464
[6] Nordheim L W 1928 *Proc. R. Soc.* A **121** 626
[7] Fowler R H and Nordheim L W 1928 *Proc. R. Soc.* A **119** 173
[8] Yuasa K, Shimoi A, Ohba I and Oshima C 2002 *Surf. Sci.* **520** 18
[9] Gadzuk J W 1964 *Phys. Rev.* **135** A794
[10] Swanson L W and Crouser L C 1967 *Phys. Rev.* **163** 622
[11] Binh Vu T, Purcell S T and Garcia N 1993 *Phys. Rev. Lett.* **70** 2504
[12] Oshima C, Matsuda K, Kona T, Mogami Y and Yamahita T 2003 *J. Vac. Sci. Technol.* B **21** 1700
[13] Gadzuk J W 1970 *Phys. Rev.* B **1** 2110
[14] Gadzuk J W 1969 *Surf. Sci.* **15** 466
[15] Nagaoka K, Yamashita T, Uchiyama S, Yamada M, Fujii H and Oshima C 1998 *Nature* **396** 557
[16] Gohda Y, Nakamura Y, Watanabe K and Watanabe S 2000 *Phys. Rev. Lett.* **85** 1750
[17] Hirose K and Tsukada M 1995 *Phys. Rev.* B **51** 5278
[18] Tada K and Watanabe K 2002 *Phys. Rev. Lett.* **88** 127601
[19] Tsukada M 1983 *Work Function* (Tokyo: Kyouritsu) (in Japanese)
[20] Lang N D and Kohn W 1970 *Phys. Rev.* B **1** 4555
[21] Skriver H L and Rosengaard N 1992 *Phys. Rev.* B **46** 7157
[22] Methfessel M, Hennig D and Scheffler M 1992 *Phys. Rev.* B **46** 4816
[23] Yamamoto S, Susa K and Kawabe U 1974 *J. Chem. Phys.* **60** 4076
[24] Gordy W and Orville Thomas W J 1956 *J. Chem. Phys.* **24** 439
[25] Gordy W 1946 *Phys. Rev.* **69** 604
[26] Wilmshurst J K 1952 *J. Chem. Phys.* **27** 1129

[27] Lafferty J M 1951 *J. Appl. Phys.* **22** 299
[28] Sato T, Yamamoto S, Nagao M, Matsukawa T, Kanemaru S and Itoh J 2003 *J. Vac. Sci. Technol.* B **21** 1589
[29] Gurney R M 1935 *Phys. Rev.* **47** 479
[30] Ishida H and Terakura K 1987 *Phys. Rev.* B **36** 4510
[31] Saargood A J, Jowett C W and Hopkins B J 1970 *Surf. Sci.* **22** 343
[32] Lemmens H J *et al* 1950 *Philips Tech. Rev.* **11** 341
[33] Levi R 1952 *US Patent* 2,700,000
[34] Zalm P and van Stratum A J A 1966 *Philips Tech. Rev.* **27** 69
[35] Swanson L W and Martin N A 1975 *J. Appl. Phys.* **46** 2029
[36] Wandelt K 1997 *Appl. Surf. Sci.* **111** 1
[37] Wiesendanger R 1994 *Scanning Probe Microscopy and Spectreoscopy* (Cambridge: Cambridge University Press)
[38] Yamada Y, Sinsarp A, Sasaki M and Yamamoto S 2003 *Japan. J. Appl. Phys.* **42** 4898
[39] Yamada Y, Sinsarp A, Sasaki M and Yamamoto S 2002 *Japan. J. Appl. Phys.* **41** 5003
[40] Sinsarp A, Yamada Y, Sasaki M and Yamamoto S 2003 *Japan. J. Appl. Phys.* **42** 4882
[41] Kondo T, Kozakai H, Sasaki T and Yamamoto S 2001 *J. Vac. Sci. Technol.* A **19** 2866
[42] Brown J K, Luntz A C and Schultz P A 1991 *J. Chem. Phys.* **95** 3767
[43] Hugosson H W, Eriksson O, Jansson U, Ruban A V, Souvatzis P and Abrikov I A 2004 *Surf. Sci.* **557** 243
[44] Kobayashi K 2000 *Japan. J. Appl. Phys.* **39** 4311
[45] Mueller W 1989 *IEEE Trans. Electron Devices* **36** 180
[46] Jenison D R, Schultz P A, King D B and Zavadil K R 2004 *Surf. Sci.* **549** 115
[47] Xiao H and Xie D 2004 *Surf. Sci.* **553** 13
[48] Lang N D and Kohn W 1971 *Phys. Rev.* B **3** 1215
[49] Smoluchowski R 1941 *Phys. Rev.* **60** 661
[50] Michelson H B 1977 *J. Appl. Phys.* **48** 4729
[51] Tagawa M, Kawasaki T, Oshima C, Otani S, Edamoto K and Nagashima A 2002 *Surf. Sci.* **517** 59
[52] Michaelides A, Hu P, Lee M H, Alvi A and King D A 2003 *Phys. Rev. Lett.* **90** 246103
[53] Delcher T A and Ehlich G 1965 *J. Chem. Phys.* **42** 2686
[54] Dushman S 1961 *Scientific Foundation of Vacuum Technology* 2nd edn (New York: Wiley)
[55] Hemenway C L *et al* 1965 *Physical Electronics* (New York: Wiley)
[56] Zhang J, Zhou W, Zhou M and Zuo T 2004 *IVESC2004: Proc. Int. Vacuum Electron Source Conf. (Beijing, China)* p 170
[57] Stackelberg M V and Neumann F 1932 *Z. Phys. Chem.* **19B** 314
[58] Broers A N 1969 *J. Phys. E: Sci. Instrum.* **2** 273
[59] Ahmed H and Broers A N 1972 *J. Appl. Phys.* **43** 2185
[60] Oshima C, Tanaka T, Bannai E and Kawai S 1977 *J. Appl. Phys.* **48** 3925
[61] Swanson L W, Gesley M and Mcneely D R 1997 *NASA Interim Report* NSG-3064
[62] Schmidt P H *et al* 1978 *J. Vac. Sci. Technol.* **15** 1554
[63] Aono M, Nishitani R, Tanaka T and Kawai S 1977 *Appl. Phys. Lett.* **31** 323
[64] Futamoto M, Nakazawa M, Usami K, Hosoki S and Kawabe U 1980 *J. Appl. Phys.* **51** 3869
[65] Swanson L W and Dickinson T 1976 *Appl. Phys. Lett.* **28** 578
[66] Futamoto M, Hosoki S, Okano H and Kawabe U 1977 *J. Appl. Phys.* **48** 3541
[67] Moss H 1968 *Narrow Angle Electron Guns and Cathode Ray Tubes* (New York: Academic)
[68] Ohuchi Y *et al* 1992 *IECE Technical Report* (Japan) ED82-89, p 43
[69] Aida T, Taguchi S, Yamamoto S and Fukushima H 1982 *J. Appl. Phys.* **53** 9029
[70] Loosjes R, Vink H J and Jansen C G J 1952 *Philips Tech. Rev.* **13** 337
[71] Rittner E S 1953 *Philips Res. Rep.* **8** 184
[72] Fomenko V S 1966 *Handbook of Thermionic Properties* (New York: Plenum)
[73] Beyar K B and Nikonov B P 1964 *Radio Eng. Electron.* **9** 1518
[74] Loosjes R and Vink H J 1949 *Philips Res. Rep.* **4** 449
[75] Rutter V E 1979 *Appl. Surf. Sci.* **2** 118
[76] Hodgeson S N B, Baker A P, Goodhand C J, van der Heide P A M, Lee T, Ray A K and Al-Ajili A 1999 *Appl. Surf. Sci.* **146** 79
[77] Gaertner G and den Engelsen D 2005 *Appl. Surf. Sci.* **251** 24
[78] Kim Y, Joo K, Choi J and Yang H 2000 *IVESC'2000 Technical Digest D4 (Orlando, FL, USA)*
[79] Ohira T *et al* 1994 *Tri-Service/NASA Cathode Workshop (Cleveland, OH, USA)*
[80] Hayashida Y, Ozawa T and Sakurai H 1999 *Appl. Surf. Sci.* **146** 7
[81] Cronin J L 1981 *IEE Proc.* **128** 19

[82] Lemmens H J, Jansen M J and Loosjes R 1949/1950 *Philips Tech. Rev.* **11** 341
[83] Huebner E 1980 *NTG Fachberichte* **71** 68
[84] Falce L R 1980 *Tri-Service Cathode Workshop*
[85] Levi R 1952 *US Patent* 2,700,000
Levi R 1965 *US Patent* 3,201,639
[86] Zalm P and van Stratum A J A 1966 *Phlips Tech. Rev.* **27** 69
[87] Kimura S, Honma K, Nikaido M, Kobayashi K, Higuchi T and Ouchi Y 1987 *Tech. Dig. Int. Electron Devices Meeting (Washington, DC)* p 689
[88] Green M C *et al* 1981 *Appl. Surf. Sci.* **8** 13
[89] Shih A *et al* 1987 *IEEE Trans. Electron Devices* **34** 2605
[90] Falce L R 1979 *US Patent* 4,165,473
[91] Schroff A and Palluel P 1979 *French Patent* 2,469,792
[92] Palluel P and Schroff A 1980 *French Patent* 2,494,035
[93] Figner A L *et al* 1967 *US Patent* 3,358,178
[94] Koppius O G 1973 *US Patent* 3,719,856
[95] van Stratum A J A 1977 *US Patent* 4,007,393
[96] van Oostrum A and Augustus L 1979 *Appl. Surf. Sci.* **2** 173
[97] Taguchi S, Aida T and Yamamoto S 1984 *IEEE Trans. Electron Devices* **31** 900
[98] Hasker J and Stoffelen H J H 1985 *Appl. Surf. Sci.* **24** 330
[99] Yamamoto S, Taguchi S, Watanabe I and Kawase S 1986 *Japan. J. Appl. Phys.* **25** 971
[100] Yamamoto S, Taguchi S, Watanabe I and Kawase S 1987 *J. Vac. Sci. Technol.* A **5** 1299
[101] Yamamoto S, Watanbe I, Taguchi S, Sasaki S and Yamamoto S 1989 *Japan. J. Appl. Phys.* **28** 490
[102] Gaertner G, Geitner P, Lydtin H and Ritz A 1997 *Appl. Surf. Sci.* **111** 11
[103] Yuan H, Gu X, Pan K, Wang Y, Liu W, Zhang K, Wang J, Zhou M and Li J 2005 *Appl. Surf. Sci.* **251** 106
[104] Yamamoto S, Yaguchi T, Sasaki S and Watanabe I 1989 *Japan. J. Appl. Phys.* **28** L865
[105] Yamamoto S, Watanabe I, Sasaki S and Yaguchi T 1990 *Vacuum* **41** 1759
[106] Yamamoto S, Taguchi S, Watanabe I and Sasaki S 1988 *Japan. J. Appl. Phys.* **27** 1411
[107] Baum W L 1980 *Appl. Surf. Sci.* **4** 374
[108] Skinner H B *et al* 1982 *J. Phys. D: Appl. Phys.* **15** 1519
[109] Haas G A *et al* 1983 *Appl. Surf. Sci.* **16** 139
[110] Norman D *et al* 1987 *Phys. Rev. Lett.* **58** 519
[111] Mueller W 1988 *J. Vac. Sci. Technol.* A **6** 1072
[112] Shih A, Hor C, Mueller D, Marrian C R K, Elam W T and Wolf P 1988 *J. Vac. Sci. Technol.* A **6** 1058
[113] Hemstreet L A, Chubb S R and Pickett W E 1988 *J. Vac. Sci. Technol.* A **6** 1063
[114] Mueller W 1991 *IEDM Technical Digest* p 399
[115] Forman R and Lesny G 1990 *IEEE Trans. Electron Devices* **37** 2595
[116] Mueller W 1997 *Appl. Surf. Sci.* **111** 30
[117] Yamamoto S, Taguchi S, Aida T, Oi T and Kawase S 1984 *Appl. Surf. Sci.* **20** 69
[118] Raju R S and Maloney C E 1994 *IEEE Trans. Electron. Devices* **41** 2460
[119] Shih A, Yater J E and Hor C 2005 *Surf. Sci.* **242** 35
[120] Liu W, Zhang K, Wang Y, Pan K, Gu X, Wang J, Li J and Zhou M 2005 *Appl. Surf. Sci.* **251** 80
[121] Gaertner G and Barrat D 2005 *Appl. Surf. Sci.* **251** 73
[122] Crewe A V, Eggenburger D N, Wall J and Walter L M 1968 *Rev. Sci. Instrum.* **39** 576
[123] Kuroda K, Hosoki S and Komoda T 1987 *J. Electron Microsc.* **36** 151
[124] Kawakubo T, Saito Y, Miyamoto M, Nakane H and Adachi H 2004 *J. Vac. Sci. Technol.* B **22** 1258
[125] Nakane H, Sato S and Adachi H 2005 *J. Vac. Sci. Technol.* B **23** 769
[126] Spindt C A 1968 *J. Appl. Phys.* **39** 3504
[127] Spindt C A, Brodie I, Humphrey L and Westerburg E R 1976 *J. Appl. Phys.* **47** 5248
[128] Gray H F *et al* 1986 *IEDM Technical Digest* 776
[129] Sarsembinov D, Yamamoto S, Itoh J, Kanemaru S and Hirano T 1995 *Technical Report of IEICE* ED95-130, p 9
[130] Yamamoto S, Saito N and Fukuhara S 1978 *Surf. Sci.* **71** 191
[131] Yamamoto S, Fukuhara S, Saito N and Okano H 1976 *Surf. Sci.* **61** 535
[132] Yamamoto S, Fukuhara S, Okano H and Saito N 1976 *Japan. J. Appl. Phys.* **15** 1643
[133] Kleint Ch 1971 *Surf. Sci.* **25** 394
Kleint Ch 1963 *Ann. Phys.* **10** 295
[134] Timm G W and Van der Ziel A 1966 *Physica* **32** 1333

[135] Gesley M A and Swanson L W 1985 *Phys. Rev.* B **32** 7703
[136] Saito Y and Uemura S 2000 *Carbon* **38** 169
[137] Hirakawa M *et al* 2000 *IDW'00* p 1027
[138] Futamoto M, Hosoki S and Kawabe U 1979 *Surf. Sci.* **86** 718
[139] Yamamoto S, Hosoki S, Fukuhara S and Futamoto M 1979 *Surf. Sci.* **86** 734
[140] Saito N 1977 *Surf. Sci.* **66** 346
[141] Toda K and Watanabe K 2002 *Phys. Rev. Lett.* **88** 127601
[142] Futamoto M, Yuito I, Kawabe U, Nishikawa O, Tsunashima Y and Hara Y 1982 *Surf. Sci.* **120** 90
[143] Adachi H, Fujii K, Zaima S and Shibata Y 1983 *Appl. Phys. Lett.* **43** 702
[144] Ishizawa Y, Aizawa T and Otani S 1993 *Appl. Surf. Sci.* **67** 36
[145] Watanbe K, Araidai M and Tada K *Thin Solid Films* **464–465** 354
[146] Cui J B and Robertson J 2002 *J. Vac. Sci. Technol.* B **20** 238